Chem Soc Rev

Tantalum-Based Semiconductors for Solar Water Splitting

Journal:	*Chemical Society Reviews*
Manuscript ID:	CS-REV-11-2013-060438.R1
Article Type:	Review Article
Date Submitted by the Author:	25-Jan-2014
Complete List of Authors:	Zhang, Peng; Tianjin University, School of Chemical Engineering and Technology Zhang, Jijie; Tianjin University, School of Chemical Engineering and Technology Gong, Jinlong; Tianjin University, School of Chemical Engineering and Technology

Tantalum-Based Semiconductors for Solar Water Splitting

Peng Zhang, Jijie Zhang, and Jinlong Gong*

Key Laboratory for Green Chemical Technology of Ministry of Education, School of Chemical Engineering and Technology, Tianjin University; Collaborative Innovation Center of Chemical Science and Engineering, Tianjin 300072, China

*Email: jlgong@tju.edu.cn; FAX: +86-22-87401818

Abstract: Solar energy utilization is one of the most promising solutions for the energy crises. Among all the possible means to make use of solar energy, solar water splitting is remarkable since it can accomplish the conversion of solar energy into chemical energy. The produced hydrogen is clean and sustainable which could be used in various areas. For the past decades, numerous efforts have been put into this research area with many important achievements. Improving the overall efficiency and stability of semiconductor photocatalysts are the research focuses for the solar water splitting. Tantalum-based semiconductors, including tantalum oxide, tantalate and tantalum (oxy)nitride, are among the most important photocatalysts. Tantalum oxide has the band gap energy that is suitable for the overall solar water splitting. The more negative conduction band minimum of tantalum oxide provides photogenerated electrons with higher potential for the hydrogen generation reaction. Tantalates, with tunable compositions, show high activities owning to their layered perovskite structure. (Oxy)nitrides, especially TaON and Ta_3N_5, have small band gaps to response to visible-light, whereas they can still realize overall solar water splitting with the proper positions of conduction band minimum and valence band maximum. This review describes recent progresses regarding the improvement of photocatalytic activities of tantalum-based semiconductors. Basic concepts and principles of solar water splitting will be discussed in the introduction section, followed by the three main categories regarding to the different types of tantalum-based semiconductors. In each category, synthetic methodologies, influencing factors on the photocatalytic activities, strategies to enhance the efficiencies of photocatalysts and morphology

control of tantalum-based materials will be discussed in detail. Future directions to further explore the research area of tantalum-based semiconductors for solar water splitting are also discussed.

1. Introduction

Solar energy is one of the most abundant natural resources, which could fulfill the energy demand of human beings if utilized effectively. As solving the problems of energy crisis and environmental issues become urgent nowadays, numerous methods have been explored to take advantages of solar energy. Among them, hydrogen production by solar water splitting has been regarded as one of the most promising directions.[1]

Compared with traditional photovoltaic methods, solar water splitting can convert solar energy into chemical energy which overcomes the incontinuous nature of solar light irradiation and realizes the storage of solar energy. Moreover, the produced chemical energy—in the form of H_2—is widely accepted as one of the most clean and sustainable energy vectors.[2]

Tremendous work have been done to obtain highly efficient photocatalysts for solar water splitting since Fujishima and Honda's seminal work in the early 1970s.[3] Unfortunately, there is still no photocatalyst that meets all the requirements for practical applications for now.[4] However, many breakthroughs have been achieved in this area, with some outstanding work on tantalum-based semiconductors. It is believed that with continues efforts hydrogen generation by solar water splitting will become one of the dominate energy supplies in the future.

From thermodynamic perspectives, the direct splitting of water into H_2 and O_2 is an uphill reaction. The Gibbs free energy, shown in the Equation 1, is 237.15 kJ/mol.[1]

Such the large energy barrier makes it urgent to find a proper photocatalyst for this reaction. Semiconductors, especially metal oxides and metal (oxy)nitrides, have been admitted as a group of important candidates for photocatalytic hydrogen production by water splitting. Two systems are normally investigated for semiconductor-based hydrogen production by solar water splitting: heterogeneous photocatalysis (HPC) and photoelectrochemical cell (PEC), as illustrated in Scheme 1.[5] In a typical HPC system, a water suspension of photocatalysts is irradiated with light, when H_2 and O_2 are generated and collected simultaneously (Scheme 1a). This system is relatively simple and has the potential to scale up for further industrial applications.[4] However, the separation of H_2 and O_2 is an important issue from the perspectives of safety and product purity, which would consume energy and lower the overall economic efficiency. Furthermore, the back reaction—H_2 and O_2 react to form H_2O—takes place once H_2 and O_2 accumulate in the system since the photocatalysts in the system are often good catalyst for the reverse reaction.[6] In the PEC system, H_2 evolution reaction (HER) and O_2 evolution reaction (OER) usually take place separately at the cathode and the anode, respectively (Scheme 1b). Notably, adding external bias or compositing with photovoltaic devices enable a larger selection of semiconductors for overall solar water splitting in the PEC system. But construction and scaling up of such system are still challenging.[6] Although some differences exist in these two systems, the essential photocatalytic mechanisms are similar.

$$H_2O \xrightarrow{hv} H_2 + 1/2\,O_2 \qquad \Delta G = +273.15\,kJ/mol \qquad (1)$$

Three different processes regarding to the formation, migration, reaction and

recombination of photogenerated charge carriers are normally present during the solar water splitting (Scheme 2a): (i) at the irradiation of light, electrons from the valence band (VB) of semiconductors are activated to the conduction band (CB), generating electron-hole pairs; (ii) the photogenerated electrons and holes migrate to the surface of the photocatalyst in the HPC system where HER and OER happen. In the PEC system, photogenerated electrons and holes will move to the cathode and anode for HER and OER, respectively; (iii) unreacted electrons and holes may meet with each other in the bulk of semiconductors and recombine, releasing energy simultaneously.[4] For each process there are some features and requirements that should be paid attention to, which will be discussed below.

For the first process, the requirement to generate electron-hole pairs is that the energy of incident light should be larger than the band gap energy of semiconductors. Thus, the absorption edges of the material can be determined by the width of band gap according to the Equation 2.[1] As an example, TiO_2—the most widely investigated semiconductor for solar conversion—has a band gap of ~ 3.2-3.4 eV, which can only response to the UV-light (with wavelength less than ~370-390 nm) of the solar spectrum.[7] Moreover, the energy of band gap should be larger than 1.23 eV to meet the thermodynamic requirement for splitting H_2O into H_2 and O_2. In practical cases, band gap energy of 1.6-2.4 eV is needed due to the energy losses at solid/liquid junctions.[1] Therefore, the width of the band gap is regarded as the very first parameter that should be considered when choosing semiconductors for solar water splitting.

$$\text{Energy of Band gap (eV)} = 1240/\lambda \text{ (nm)} \qquad (2)$$

Before undergoing the reactions in the process ii, charge carriers need to migrate to the surface of photocatalysts or electrodes. In order to make this process more efficient, constructing nanomaterials, crystal structure/crystallinity controlling, doping and many other approaches are considered to be beneficial. Materials with nanostructures can shorten the migration distance of charge carriers and increase the possibilities of electrons and holes reaching to the surface owing to the small dimensions and large surface area;[8] crystal structure/crystallinity controlling and doping are good approaches to enhance the conductivity of semiconductors resulting in improved transportation of charger carriers. Hematite, for instance, appears to be a promising candidate for solar hydrogen production since it is stable, abundant and responsive to visible light. However, it surfers from the short lifetime of activated charge carriers which can be overcome to some extent by controlling the morphology and taking advantage of nano-construction.[9, 10]

When the electrons and holes move to the surface of catalysts, two half reactions are expected. In order to have the two half reactions happen simultaneously, the conduction band minimum (CBM) and valence band maximum (VBM) of semiconductors must straddle the redox potential of H^+/H_2 (0 V vs. NHE) and O_2/H_2O (1.23 V vs. NHE) as shown in Scheme 2b.[4] However, some materials including WO_3 do not have suitable band gap positions for both half reactions. As the CBM of WO_3 is lower than the hydrogen redox potential, a sacrificial agent (electron acceptor like Ag^+ in this case) is usually added to consume electrons and leave holes for OER in the HPC system. Another solution is to construct Z-scheme system which is composed of

two photocatalysts that are active for OER and HER separately.[11] The two photocatalysts are integrated by a redox pair that is also called electron mediator to realize the overall solar water splitting. In the PEC system, an external bias is usually applied to achieve this goal.

In addition to overcome thermodynamic limits, cocatalysts—acting as surface reaction sites—are always used to enhance the activities of semiconductors. Cocatalysts are metals or metal oxides that are used together with photocatalysts to help enhance the photocatalytic efficiency. For example, IrO_2 and Pt are regarded as outstanding cocatalysts to improve the ability of semiconductors towards OER and HER, respectively. However, excess loading of cocatalysts will induce more recombination centers for the process iii which is unfavorable in photocatalysis process.[12]

Additionally, crystal defects, dopants, vacancies, *etc.* can also act as recombination centers for photogenerated electrons and holes in the process iii. Therefore, work has been done to improve the degree of crystallinity and to control the impurity in semiconductor-based photocatalysts. Some other strategies have also been tried to restraint the recombination. Constructing of heterojunction (the interface between different semiconductors), for instance, can effectively enhance the separation of charge carriers.

It is apparent that an appropriate band gap structure plays the primary role for good catalytic performance. Additionally, the abundance, stability, cocatalysts, conductivity and many other factors are relatively important. Tantalum-based

semiconductors, as a relatively new category of photocatalysts, satisfy most of the requirements for good photocatalysts and have shown high efficiencies in the solar water splitting.

One of the most important advantages of tantalum-based semiconductors is that their band gaps are suitable for overall solar water splitting. Compared with some traditional photocatalysts such as TiO_2, the CBM of tantalum oxide is higher, which indicates the larger potential for photogenerated electrons to undergo HER. Compared with some similar transition metal oxides such as ZrO_2 (with a band gap of ~5.0 eV),[4] tantalum oxide has a smaller band gap which could absorb a larger range of incident light. The layered perovskite structure of tantalates makes them highly active for the solar water splitting. The visible-light responsiveness of tantalum (oxy)nitrides provides a much higher theoretical efficiency which guarantees their potential to be used in practical applications. The outstanding features of tantalum-based semiconductors make them to be promising candidates for hydrogen generation by solar water splitting.

This review describes the design, synthesis, and applications of tantalum-based semiconductors in both solar water splitting systems. It will be divided into three categories focusing on tantalum oxide, tantalates and tantalum (oxy)nitrides, followed by the perspective. For more detailed information about solar water splitting, readers can refer to some excellent reviews published recently.[1, 4-8, 13, 14] Limited discussion on some tantalum-based semiconductors can also be found in parts of reviews.[1, 4, 5, 11, 15-19] This review provides a comprehensive and inspiring summary of tantalum-based

semiconductors for solar water splitting.

2. Tantalum Oxide

Tantalum oxide—referring to tantalum pentaoxide with the formula Ta_2O_5—was first used as an antireflective layer material in optical and photovoltaic devices. Then it became well known as a dielectric material in electronic industry owing to its high dielectric constant of more than 20.[20] As a semiconductor material for photocatalytic reactions, Ta_2O_5 has a band gap of ~3.9 eV, the VBM and CBM of which straddle the redox potentials of H^+/H_2 and O_2/H_2O.[21] This feature makes Ta_2O_5 a promising material for overall solar water splitting. Moreover, the CBM of Ta_2O_5 is more negative comparing with some traditional photocatalysts such as TiO_2, which makes the HER happen more easily. Ta_2O_5 was first investigated as a photocatalyst for noticeable hydrogen generation by solar water splitting in 1994 by Sayama and Arakawa when it was integrated with RuO_2 or NiO_x cocatalysts.[22] Subsequently, the research of Ta_2O_5 for solar water splitting had been conducted widely and developed into three strategies.

Firstly, different synthetic methods were widely investigated in order to get Ta_2O_5 photocatalysts with large surface areas and small dimensions. Secondly, different approaches were tried to address the issue that the large band gap of Ta_2O_5 makes it only responsive to UV-light, the energy of which is only about 4% of the whole solar spectrum as mentioned earlier on. Integrating other visible-light-responded semiconductors with Ta_2O_5 and doping extern ions to the bulk

were regarded as reasonable solutions. Finally, the catalytic activity of Ta_2O_5 could be improved by finely tuning its morphology. All these three strategies will be discussed in detail below. Relevant research on the design of Ta_2O_5 photocatalysts is summarized in Table 1.

2.1 Synthetic methodologies of Ta_2O_5

Early work had been focused on developing the synthetic methods for Ta_2O_5 photocatalysts with large surface areas and high activities. Ta_2O_5 obtained by a solvothermal method with post-calcination showed a β-phase crystal structure. By using such the β-Ta_2O_5 photocatalyst in the HPC system with 2-propanal as a sacrifice agent, the highest hydrogen generation rate of 610 μmol/h·g was detected.[23]

A ligand-assisted templating method was conducted to obtain mesoporous Ta_2O_5 by Domen's group. Upon loading of NiO cocatalyst, the mesoporous NiO-Ta_2O_5, with pretreatment of sequent H_2 reduction and O_2 reoxidation showed an improved activity for overall solar water decomposition.[24] The H_2 and O_2 generation rates were 1030 μmol/h·g and 544 μmol/h·g, respectively. This ligand-assisted templating method was widely adapted to synthesize mesoporous Ta_2O_5.[25] The high activity of mesoporous Ta_2O_5 originated from its thin structure that reduced the migration distance of charge carriers to the surface active sites. However, the amorphous nature of mesoporous Ta_2O_5 limited its application. High temperature annealing could improve its crystallinity but resulted in the decrease of surface area with collapsed structure. In order to solve this problem, SiO_2 reinforcement was added to synthesize crystalize

two-dimensional hexagonal mesoporous Ta_2O_5 as shown in Fig. 1a. The excellent photocatalytic property when it is loaded with NiO_x was due to the thin-wall crystalline phase, which provided reduced transfer pathway and better conductivity for charge carriers.[26]

Loading of cocatalysts to semiconductors leads to the formation of defects, which frequently act as recombination centers for electro-hole pairs. Therefore, controlling of the cocatalyst-semiconductor interface is an urgent task to reduce the number of defects. Moreover, a clear cocatalyst-support interface will also enhance the transport of charge carriers and thus improve the catalytic activity. It was claimed that the use of cold plasma pretreatment method provided a clear and well-defined metal-support interface without diffused interfacial region, which led to an enhanced activity, comparing with the traditional method with thermal decomposition of metal salt (Fig. 1b, c). It was suggested to be ascribed to the avoidance of migration of Ni atom to the bulk of Ta_2O_5.[27]

The combination of co-precipitation and hydrothermal methods in a NH_4F medium resulted in the formation of nanoporous Ta_2O_5 spheres with surface fluorination.[28] The surface F species acts as electron-trapping site sand restricted the recombination of charge carriers, which led to a superior photocatalytic properties comparing with P25 and commercial Ta_2O_5.

The synthetic methods of Ta_2O_5 photocatalysts with controllable morphology have been widely explored. Freestanding Ta_2O_5 nanotubes had been fabricated by increasing the temperature of electrolyte to 50 ^oC during the anodization process as

shown in Fig. 1d.[29] Annealing at temperatures higher than 750 °C could increase the crystallinity of the materials. An increased photocatalytic hydrogen production rate from an aqueous ethanol solution under UV-light irradiation was detected with such the Ta_2O_5 nanotubes mainly owing to its high crystallinity. Ta_2O_5 hollow spheres were synthesized by a layer-by-layer adsorption method using polystyrene (PS) spheres as the template (Fig. 1e).[30] The obtained Ta_2O_5 hollow spheres yielded a hydrogen generation rate 20 times higher than that of commercial Ta_2O_5 powders owing to the large surface area, high crystallinity, and ultrathin topology. Another method using nonionic triblock copolymer F127 as the structure-directing agent and $Ta(OC_4H_9)_5$ as the precursor had also been conducted to synthesize Ta_2O_5 hollow spheres.[31] The hollow Ta_2O_5 spheres showed enhanced photocatalytic hydrogen production stability from aqueous methanol solution with core-shell Ni/NiO particles as a cocatalyst comparing with bulk Ta_2O_5. The unstable activity of bulk Ta_2O_5 might be the result of particle aggregation which is supported by the change of surface area.

2.2 Doping and constructing heterojunctions

In order to enhance the photocatalytic activities of Ta_2O_5, different approaches, including doping and constructing heterojunctions, have been conducted. It was claimed that doping Ta_2O_5 with transition metal ions or integrating Ta_2O_5 with other semiconductors having small band gaps were useful ways to increase its visible-light responsibility. The activity of Ta_2O_5 could also be enhanced by constructing heterojunctions, which promoted the separation of electrons and holes.

Doping Fe^{3+} into the matrix of Ta_2O_5 had been realized by both sol-gel and solid reaction methods to synthesize Fe-doped mesoporous and non-porous bulk Ta_2O_5, respectively.[32] The two kinds of photocatalysts showed red shift of the absorption edges to the visible range.

The incorporation of In_2O_3 could effectively improve the thermal stability of mesoporous Ta_2O_5 and enhance its photocatalytic efficiency by forming heterojunctions.[33, 34] Improved activity and stability of photocatalytic hydrogen generation from simulant waste water had been detected by using photocatalyst with heterojunctions between quantum-sized CdS and Ta_2O_5.[35, 36] This was because of the visible-light absorption and the accelerated transfer of photogenerated charge carriers by introducing potential gradient between CdS and Ta_2O_5 as both the VBM and CBM of Ta_2O_5 are more positive than those of CdS.

Although Ta_2O_5 has the band gap structure suitable for overall solar water splitting, it can only utilize UV-light and surfers from a relatively low photocatalytic efficiency which hinders its further development. Among all the trials to improve the photocatalytic activity of Ta_2O_5, the designing and constructing of tantalates is considered to be a very useful way, which will be discussed in the next section.

3. Tantalates

Broadly defined herein, tantalates represent a group of materials that consist of TaO_3^-, $Ta_2O_6^{2-}$ and other relative tantalum-containing anions together with metal cations including alkali, alkaline earth, transition and some other main group metals.

Typically, tantalates with different surface morphologies and bulk compositions are synthesized by the high-temperature solid-solution method, together with hydrothermal, sol-gel and other methods. As a category of photocatalysts for solar water splitting, tantalates have relatively high activities due to their unique layered structure that can facilitate the migration of charge carriers. However, the large band gap hinders their usage under visible-light irradiation. A variety of approaches have been proposed to solve this problem including doping and dye sensitization.

The majority of investigations on tantalate photocatalysts for solar water splitting focus on the HPC system, whereas limited work is relevant with the PEC system. Both systems will be discussed in detail in this section. Specifically, tantalates in the HPC system can be further classified into alkali tantalates, alkaline earth tantalates and other tantalates according to the sort of cations they contained. Relevant research of the tantalates in the HPC system is summarized in Table 2.

3.1 Alkali Tantalates

3.1.1 Synthetic methodologies of alkali tantalates

The solid-state reaction is the most common method to synthesize alkali tantalates, which involves the high temperature treatment of the mixture of Ta_2O_5 and alkali salts. In 1996, a seminal work demonstrated the solar water splitting properties of Ni intercalated $KTaO_3$ and $Rb_4Ta_6O_{17}$ in the HPC system, which were obtained by the solid-state reaction method,.[37] $LiTaO_3$, $NaTaO_3$ and $KTaO_3$, synthesized with the same method, were reported to exhibit the photocatalytic ability to decompose water

into stoichiometric H_2 and O_2 by Kudo and coworkers.[38] Among all the materials, $KTaO_3$ showed the highest activity.

An improved solid-state reaction synthetic method with an excess amount of alkali to compensate the volatilization was conducted.[39, 40] All the $LiTaO_3$, $NaTaO_3$ and $KTaO_3$ catalysts synthesized by such the method had enhanced activities comparing with catalysts that were prepared in a stoichiometric ratio of precursors. This was due to the fine structure of the grown crystal as well as the suppression of defects formation. Both factors would reduce the recombination of electrons and holes and thus increase the photocatalytic activities. The trend of activities for catalysts obtained with the excessive alkali was $KTaO_3 < NaTaO_3 < LiTaO_3$. $LiTaO_3$ showed the best performance since it had a more negative CBM and a higher transferring excited energy induced by the small Ta-O-Ta angel (143^o) (Fig. 2). Upon loading of cocatalysts, NiO-$NaTaO_3$, however, showed the highest activity. The improved separation of photogenerated charge carriers was ascribed to the alignment of CBMs of NiO and $NaTaO_3$ (Fig. 2b). But the enhancement of NiO cocatalyst for $LiTaO_3$, with the same band gap alignment, was not significant mainly due to the partly doping of Li^+ ions to NiO.[41] The work on NiO-$NaTaO_3$ for hydrogen production by solar water splitting led to numerous investigations regarding the synthetic methods and origin of photocatalytic properties of $NaTaO_3$.

One should note that $NaTaO_3$ synthesized by the hydrothermal method exhibited an 8 times higher activity (H_2 and O_2 generation rates of 26.7 and 13.7 mmol/h·g, respectively) compared to the catalyst obtained by the conventional solid-state

reaction method owing to its smaller particle size, larger surface area and higher crystallinity.[42, 43] A microwave-assisted hydrothermal method can further decrease the synthetic time and improve the activity of the $NaTaO_3$ photocatalyst. Pretreatment of Ta_2O_5 powders by ball milling can promote the dissolution process in such the hydrothermal method, which would change the reaction pathway from direct conversion ($Ta_2O_5 \rightarrow NaTaO_3$) to indirect conversion ($Ta_2O_5 \rightarrow Na_2Ta_2O_6 \rightarrow NaTaO_3$) with the formation of intermediate pyrochlore $Na_2Ta_2O_6$ phase. Such the indirect reaction pathway had a lower thermodynamic energy and resulted in the formation of pure perovskite-type $NaTaO_3$ with a high crystallinity and a large surface area. Therefore, it showed the photocatalytic water splitting activity two times greater than that of the catalyst synthesized by the hydrothermal method.[44]

By adding cetyltrimethyl ammonium bromide (CTAB) as a templating agent and tantalum ethoxide as a precursor during the hydrothermal synthetic process, $Na_2Ta_4O_{11}$ was successfully synthesized with an outstanding activity for hydrogen generation by photocatalytic water splitting.[45] Another template-assisted hydrothermal approach was conducted by the Domen's group to synthesize colloidal arrays of $NaTaO_3$.[46] Three-dimensional mesoporous carbon was first fabricated by using cubic close packed silica nanospheres as the template. Moreover, the size of the silica nanospheres can be tuned to get the mesoporous carbon with different pore dimensions. Then the colloidal arrays of $NaTaO_3$ were synthesized by the hydrothermal method with the reaction between Ta_2O_5 and NaOH in the pores of the carbon template, which was removed afterwards. It was claimed that the addition of

poly(vinylpyrrolidone) (PVP) and ethylene glycol (EG) was important to realize the controllability of the size and shape of $NaTaO_3$. The colloidal arrays consisted of 20 nm $NaTaO_3$ nanoparticles showed a very good activity (H_2 generation rate of 6.67 mmol/h·g and O_2 generation rate of 3.33 mmol/h·g), which was three times higher than the activities of samples obtained without using the carbon replica.

Different synthetic methods had also been conducted to attain alkali tantalates with different crystal structures. $Na_2Ta_2O_6$ and $K_2Ta_2O_6$ pyrochlores were synthesized by the hydrothermal method, which showed relatively high activities with NiO as a cocatalyst.[47] Hydrothermal method with $NaTa(OC_3H_7)_6$ as a sole precursor and NH_3 as a base catalyst resulted in the formation of $Na_2Ta_2O_6$ with an average particle size of 25 nm; the catalyst showed a better activity than that of amorphous porous $NaTaO_x$ and crystalline $NaTaO_3$.[48] $K_2Ta_2O_6$ with pyrochlore-like cubic crystal structure was also synthesized by the hydrolysis of K-Ta mixed ethoxides.[49] Compared with perovskite-structured $KTaO_3$, $K_2Ta_2O_6$ had much higher photocatalytic activity mainly due to the larger surface area as well as the smaller crystalline size (approximately 30 nm). It is likely that the charge separation in the $K_2Ta_2O_6$ crystal is more facile than $KTaO_3$ owing to the local polarization effects since the TaO_6 octahedral unit is much distorted in K_2TaO_6 (Fig. 3).

Teng's group employed the sol-gel method to synthesize $NaTaO_3$ at 500 ^oC.[50] The low synthetic temperature resulted in the monoclinic crystal structured $NaTaO_3$ rather than the orthorhombic phase obtained from solid-state reaction. Density functional theory (DFT) calculations indicated that monoclinic $NaTaO_3$ with an

indirect band gap, which would involve the photon absorption and emission during the photocatalytic process, had a lower recombination rate of electron-hole pairs. Additionally, the density of states (DOS) sharply rose near the CB and VB of monoclinic $NaTaO_3$, indicating more effective states for photogenerated electrons and holes. The bond angel of Ta-O-Ta was close to 180^o in the monoclinic crystal structure (Fig. 4), which indicated a higher mobility of charge carriers. These factors account for the higher activity of monoclinic $NaTaO_3$. A followed research was conducted to further understand the relationship between the bond angel of Ta-O-Ta in $NaTaO_3$ and catalytic properties.[51] Both solid-state and hydrothermal methods resulted in the formation of orthorhombic crystal structure of $NaTaO_3$. However, the sol-gel method led to the formation of the monoclinic structure. And the band angels of Ta-O-Ta were 157^o, 163^o and 179^o for $NaTaO_3$ synthesize by solid-state, hydrothermal and sol-gel methods, respectively. It was claimed the delocalization of photogenerated electrons was affected by the band angel of Ta-O-Ta. When the angel was close to 180^o, the mobility of charge carrier would be enhanced and thus the photocatalytic activity would be improved. Both the apparent and the surface-area-normalized H_2 generation rates were in accordance with the argument.

3.1.2 Alkali tantalates with pillared structures

$K_3Ta_3Si_2O_{13}$ with a one-dimensional pillared structure had been reported to effectively decompose water into stoichiometric amount of H_2 and O_2 by Kudo's group.[52] This $K_3Ta_3Si_2O_{13}$ catalyst was constructed by three corner-sharing TaO_6 linear chains, which were linked by Si_2O_7 ditetrahedral with potassium filled in the

pentagonal tunnel space (Fig. 5a). It was claimed that the photocatalytic activity of $K_3Ta_3Si_2O_{13}$ was relevant with the electron or/and energy migration in the one-dimensional structure with respect to the TaO_6 chain. $K_3Ta_3B_2O_{12}$ with a similar crystal structure as $K_3Ta_3Si_2O_{13}$ was consisted of TaO_6 pillars connected by BO_3 triangle units (Fig. 5c). It exhibited a high activity (H_2 generation rate of 4.8 mmol/h·g and O_2 generation rate of 2.4 mmol/h·g) for water splitting even without cocatalyst.[53] An improved synthetic method by using a water-soluble Ta-peroxolactate complex through an aqueous solution-based process was conducted to obtain $K_3Ta_3B_2O_{12}$ instead of the traditional solid-state reaction.[54] Such the method would prevent the formation of volatile boron compounds and thus reduce boron deficiency. The corner-sharing of the TaO_6 octahedra in $K_3Ta_3Si_2O_{13}$ and $K_3Ta_3B_2O_{12}$ leads to the adjustment of Ta-O-Ta angel to be close to 180°, which would result in an increase of the probability for excited charge carriers to reach the active sites for HER and OER.

Inspired by such the idea, $K_2LnTa_5O_{15}$ (Ln indicates lanthanides) with the tungsten bronze structure was synthesized (Fig. 5b), which contained corner-sharing TaO_6 units.[55] Among the catalysts synthesized, $K_2PrTa_5O_{15}$ and $K_2SmTa_5O_{15}$ showed high activities. $K_2EuTa_5O_{15}$ and $K_2YbTa_5O_{15}$ showed relatively lower activities probably because that Eu and Yb acted as electron trapping sites. However, $K_2CeTa_5O_{15}$, which had fairly low activity, showed the ability to absorb visible-light. Shangguan and coworkers further investigated the same catalyst, which exhibited the absorption edge of about 540 nm, corresponding to a band gap energy of 2.3 eV.[56] From DFT calculations, O 2p, Ta 5d and occupied Ce 4f orbitals were responsible for

the VB which showed a negative shift and resulted in the smaller band gap energy, whereas the CB were mainly attribute to the Ta 5d orbitals. It was also observed that unoccupied Ce 4f orbitals overlap with the CBM, but their high localized nature made them less effective in the photocatalysis process.

3.1.3 Alkali tantalates with layered perovskite structures

Tantalates with the formula of $AA'Ta_2O_7$ (A = alkali metal or H, A' = lanthanides) has drew a great deal of attention for their layered perovskite structure and considerable photocatalytic properties. Machida and coworkers had conducted a systematic investigation of such the tantalate photocatalysts. Among the $RbLnTa_2O_7$ (Ln = La, Pr, Nd and Sm) catalysts investigated, $RbNdTa_2O_7$ showed the highest photocatalytic activity to decompose water into stoichiometric H_2 and O_2 under UV-light irradiation in the absence of cocatalysts.[57] Moreover, an improved activity (H_2 and O_2 generation rate of 586.0 and 293.5 μmol/h·g, respectively) was detected when it was loaded with small amount (0.5 wt.%) of Ni cocatalyst.[58] According to VB X-ray photoelectron spectroscopy (XPS) measurements and first-principles calculations of the band structure using the all-electron full-potential linear augmented plane-wave (FLAPW) method, two possible explanations to the high activity of $RbNdTa_2O_7$ were proposed.[59] Firstly, the degree of the Ln-O-Ta hybridization, affecting the position of CB and VB as well as their DOS, was responsible for the differences of photocatalytic activity. The unoccupied Nd 4f orbitals did not contribute to the CB, which was consisted of O 2p and Ta 5d. This feature allowed the smooth migration of photoexcited electrons. The other reason was that the

hybridization of occupied Nd 4f orbitals with O 2p orbitals could increase the DOS of VB thus enhance the efficiency of excitation of electrons to the CB (Fig. 6a). These claims were further proved by testing the catalytic properties of a series of AA'Ta_2O_7 photocatalysts with the A site as Cs, Rb, Na, H and the A' site as La, Pr, Nd, Sm.[60] Notably, the optical band gap energy mainly depended on the content of Ln. However, both the Ln and A sites would affect the photocatalytic activity as shown in Fig. 6b. $RbNdTa_2O_7$ remained the highest activity owing to its appropriate band gap structure. The effect of hydrated interlay for catalysts with Na and H cations was also studied. The hydrated Na phase showed enhanced activity when it was loaded with Ni cocatalyst owing to improved mobility of molecular water within the interlay for its reversible hydration/dehydration behavior, whereas the H ion exchanged catalysts were not effective without such the effect.

Shimizu and coworkers had conducted a series of investigations on Ruddlesden-Popper-type double-layered perovskite tantalates with the formula as $A_2A'Ta_2O_7$ (A = alkali metal or H; A' = alkaline earth metal or lanthanides). Among the $A_2SrTa_2O_7{\cdot}nH_2O$ (A=H, K, Rb) and $Li_2SrTa_2O_7$ photocatalysts, $H_2SrTa_2O_7{\cdot}nH_2O$ and $K_2SrTa_2O_7{\cdot}nH_2O$ with the hydrated interlayer showed relatively higher photocatalytic activities to split water into H_2 and O_2 without cocatalyst.[61] The authors hypothesized that the existence of the hydrated interlayer played an important role in maintaining high activities. For hydrated catalysts, electro-hole pairs could easily migrate to the interlayer surface where intercalated H_2O molecules located. The reaction of charge carriers with H_2O molecules rather than the recombination would

dominate. This claim had been proved by a photoluminescence spectroscopy study in the HPC system with sacrificial agents.[62] Hydrated layered tantalates showed lower luminescence efficiency indicating that the photogenerated charge could be trapped by interlayered water, which was in accordance with the hypothesis. N-butylamine was used as the sacrificial agent, which could be absorbed into the interlayer space of H^+-exchanged layer oxides ($H_2SrTa_2O_7 \cdot nH_2O$ in this case) while not for $K_2SrTa_2O_7 \cdot nH_2O$. The higher hydrogen generation rate for $H_2SrTa_2O_7 \cdot nH_2O$ in *n*-butylamine solution comparing with $K_2SrTa_2O_7 \cdot nH_2O$ indicated that the reaction proceeded at the interlayer of hydrated layered tantalates.

$A_2La_{1/3}Ta_2O_7$ (A = K and H) had lower activities comparing with A_2SrTaO_7. However, when loaded with Ni species as a cocatalyst by an ion-exchange method, the hydrogen generation rate of the $H_2La_{1/3}Ta_2O_7$ was 6 times larger than that of the unloaded catalyst, while such the enhancement was not achieved on $H_2SrTa_2O_7$.[63] From extended x-ray absorption fine-structure spectroscopy (EXAFS)/x-ray absorption near-edge spectroscopy (XANES), UV-visible spectroscopy, and TEM results, it was concluded that Ni species, in the form of Ni^{2+} ions and small NiO clusters, were intercalated into the interlayer for $H_2La_{1/3}Ta_2O_7$, whereas larger NiO particles were present at the surface for $H_2SrTa_2O_7$. The highly dispersed Ni(II) species, as the H_2 formation centers, shortened the migration distance of photogenerated electrons, thus enhancing the activity of $H_2La_{1/3}Ta_2O_7$. However, the large NiO particles did not participate in the reaction for $H_2SrTa_2O_7$.

$ACa_2Ta_3O_{10}$ (A = alkali metal, H and $C_6H_{13}NH_3$) triple-layered perovskite

tantalates were also regarded as effective photocatalysts for hydrogen generation by photocatalytic decomposition of H_2O. The investigation of different catalysts (with A = Cs, Na, H, and $C_6H_{13}NH_3$) showed that the hydrated Na phase had the highest activity with NiO_x as cocatalyst.[64] The interlayer had been regarded as the active sites for photocatalytic reactions, which was confirmed by H_2O/D_2O isotopic experiments. Therefore, the high mobility of water molecules within the interlayer due to the reversible hydration/dehydration behavior of $NaCa_2Ta_3O_{10}$ resulted in its high activity. Hence, the hydration behavior was considered to be a primary factor affecting the photocatalytic activity associated with the enthalpy of hydration (ΔH_h^o). The Cs phase with the smallest ΔH_h^o was unfavorable for the hydration both in vapor and liquid phases. However, the Li phase formed an anhydrous phase even if it had a large ΔH_h^o. A hydrothermal treatment had been successfully conducted to synthesize hydrated $LiCa_2Ta_3O_{10}$ which showed the highest activity among the $ACa_2Ta_3O_{10}$ tantalates (with the A site as alkali metals).[65]

In order to further understand the role of interlayer hydration, $K_{1-x}Na_xCa_2Ta_3O_{10}\cdot nH_2O$ and $Li_{1-x}Na_xCa_2Ta_3O_{10}\cdot nH_2O$ photocatalysts with various x values had been synthesized by ion exchange of $CsCa_2Ta_3O_{10}$ in mixed molten nitrates.[66] The amount of interlayered water was in accordance with the Na content (which could as be considered as x value). For the $K_{1-x}Na_xCa_2Ta_3O_{10}\cdot nH_2O$ catalyst, the activity increased in consistent with the interlayer water content. However, the highest photocatalytic activity for $Li_{1-x}Na_xCa_2Ta_3O_{10}\cdot nH_2O$ was obtained at x = 0.77 with H_2 and O_2 generation rates of 3.4 and 1.6 mmol/h·g, respectively. These results

indicated that the interlayered water was not the only factor for the catalytic activity. Li ions at the interlayer may also play a key role in solar water splitting. The activity of $LiCa_2Ta_3O_{10}$ loaded with Ni cocatalyst could be improved by thermal treatment.[67] Such the improvement was mainly because of a decrease in the thickness in triple-layered perovskite slab, leading to an increase of dipole movement of TaO_6 octahedron with enhanced separation efficiency of charge carriers.

3.1.4 Doping of metal cations

Doping has been widely employed to improve photocatalytic activities of alkali tantalates. Earlier work focused on doping a small amount of cations including Zn^{2+}, Y^{3+}, Al^{3+}, Ga^{3+}, In^{3+}, Ce^{4+}, Ti^{4+}, Zr^{4+}, Si^{4+}, Ge^{4+}, Nb^{5+}, Sb^{5+} and W^{6+} into $KTaO_3$.[68] It was observed that the Hf^{4+}, Zr^{4+} and Ga^{3+} doped $KaTaO_3$ showed improved hydrogen generation activities. Further investigation of Zr^{4+} doped $KTaO_3$, which showed ability to decompose H_2O into stoichiometric H_2 and O_2, concluded that the increased lifetime of charge carriers was responsible for the enhanced activity. Detailed examination on Hf^{4+} and Ti^{4+} doped $KTaO_3$ revealed the similar mechanism that group 4 elements can act as charge carrier annihilators to decrease the electrical conductivity of $KTaO_3$ and lengthen the exit time of charge carriers.[69]

$NaTaO_3$ photocatalysts doped with lanthanides (including La, Pr, Nd, Sm, Gd, Tb and Dy) was also synthesized and applied to solar water splitting by Kudo and coworkers.[70] Among all these catalysts, La-doped $NaTaO_3$ showed the highest activity with H_2 and O_2 generation rates of 5.9 and 2.9 mmol/h·g, respectively. Further studies revealed that doping of La can decrease the particle size and increase the crystallinity

of $NaTaO_3$. These effects would suspend the recombination of charge carriers, indicating that more electrons and holes reached the surface and reacted with H_2O molecules. The effect of La dopant had also been studied by time-resolved infrared absorption spectroscopy (IRAS).[71] The replacement of one Na^+ ion with one La^{3+} ion would result in the loss of two more Na^+ ions to keep the balance of ionic charge. Thus, the modulation of electrostatics at the replaced lattice would enhance the separation of charge carriers. The electrostatic potential gradient formed from the surface to the bulk owing to the preferential distribution of La^{3+} at the surface may also promote the charge separation. Moreover, the characteristic nanostep structure (Fig. 7) as a result of La doping can effectively separate HER and OER sites. The HER, with H_2 generation rate of 19.8 mmol/h·g, would take place at the edge where ultrafine NiO nanoparticles were located. However, the OER would occur at the grooves. Such the groove geometry with walls on both sides can provide multi-hole injection sites to accomplish four electrons oxidation and complex molecular combination and thus enhance the OER with O_2 generation rate of 9.7 mmol/h·g.[72]

A green H_2O_2 assisted sol-gel method had also been conducted to synthesize La-doped $NaTaO_3$ which showed high activity, crystallinity and anti-aggregation stability.[73] Loading of nickel-based cocatalysts can further increase its activity.[74]

Similar results had also been achieved by doping alkaline earth metal ions (Ca, Sr, and Ba) into $NaTaO_3$.[75-77] Small particle size, high crystallinity and formation of surface nanosteps, as results of alkaline earth metal ions doping, were beneficial for improving the photocatalytic activity of $NaTaO_3$. It was also observed that a large

amount of dopant would result in the decrease of the activity mainly because of the formation of defects acting as the recombination centers.

Doping of transition metal cations had also been proved to enhance the salability of alkali tantalates. Nanocubic (Na, K)TaO_3 synthesized by the convenient molten-salt process showed a good activity without cocatalyst (H_2 generation rate of 25.1 mmol/h·g). However the stability was low due to the formation of peroxidation phase. When doped with Zr^{4+} or Hf^{4+} ions, the catalysts became more stable due to the prolonged lifetime of photo-excited charges. The activity had also been improved with doping of Zr^{4+} or Hf^{4+} ions (H_2 generation rate of 46.5 and 49.6 mmol/h·g for Zr^{4+} and Hf^{4+} dopants, respectively)[78]

3.1.5 Activity enhancement under visible-light irradiation

Since most alkali tantalates have small band gaps and can only absorb UV-light, improving their visible-light responsiveness could be a promising method to enhance their photocatalytic activities due to the higher solar light utilization efficiency. Different approaches including dye sensitizing and doping of external ions have been tried.

Surface modification with organic dyes (e.g., cyanocobalamin, Co-phthalocyanine and Co-tetraphenylporphyrin) to the Zr^{4+} doped $KaTaO_3$ can enhance its photocatalytic activity. This was because of the improved visible-light absorption and charge separation efficiency by testing the photovoltaic potential upon irradiation.[79] The lowest unoccupied molecular orbital (LUMO) energy level played an important role in the enhancement of different organic dyes. A volcano type

dependence (Fig. 8) of H_2 formation rate to LUMO of dye was observed, which indicated the optimum LUMO level was -0.9 V vs. NHE.[80]

Introducing external metal ions has been widely adopted as an effective way to enhance the photocatalytic activity under visible-light irradiation of semiconductors with large band gaps. Doping $NaTaO_3$ with transition metals, such as Cu, can effectively improve its visible-light responsiveness as Cu 3d orbit can contribute to the VB and reduce the band gap. A small amount of Cu dopant can act as trapping sites to inhibit the recombination of charge carriers. The characteristic structure of $NaTa_{0.92}Cu_{0.08}O_3$ can provide more active sites and thus enhance the photocatalytic activity.[81] Ir doped $NaTaO_3$ can also absorb visible light upon co-doped with alkali earth metals or lanthanum ions.[82]

$Na(Bi_xTa_{1-x})O_3$ obtained by the hydrothermal method showed visible-light photocatalytic activities.[83] The hybrid CB consisted of Bi 2s, Bi 2p and Ta 5d orbitals accounted for the visible-light responsiveness. $H_{1.9}K_{0.3}La_{0.5}Bi_{0.1}Ta_2O_7$ with a layered perovskite structure was obtained by H ion-exchange of $K_{0.5}La_{0.5}Bi_2Ta_2O_9$ in acid solutions. It possessed superior activity with H_2 generation rate of 2.7 mmol/h·g in the absence of cocatalysts comparing with its parent materials.[84] The excellent activity was originated from the more negative CB, driven from the exfoliation of Bi during the protonated process, and layered structure upon acid treatment.

Doping of non-metal elements is an alternative way to improve the visible-light responsiveness of semiconductor photocatalysts. N-doped $CsCa_2Ta_3O_{10}$ had been synthesized, which showed enhanced O_2 generation ability under visible light

irradiation comparing with the undoped catalyst.[85]

3.1.6 Cocatalysts

Nickel species have been widely investigated as the cocatalysts for alkali tantalates. Some other cocatalysts including Au nanoparticles, RuO_2, and $[Mo_3S_4]^{4+}$ have also been employed to improve the photocatalytic activities of tantalates for water splitting.

Loading Au nanoparticles onto different tantalates by the photodeposition method had been conducted.[86] Examination of Au-loaded La-doped $NaTaO_3$ in different sacrificial regents (to sacrifice photogenerated electrons or holes) demonstrated that Au cocatalyst acted as the active sites for H_2 generation. One should note that the deactivation of the Au loaded photocatalyst was due to the photoreduction of O_2 at under-coordinated Au sites rather than the back reaction between generated H_2 and O_2. By using the impregnation method to load Au nanoparticles, the stability can be improved.[87] It was due to the large spherical Au nanoparticles obtained by the impregnation method; they had relatively smaller periphery of the interface between Au and La-doped $NaTaO_3$ (Fig. 9b), which is crucial for O_2 activation comparing with the catalyst obtained by the photodeposition method (Fig. 9a). La-doped $NaTaO_3$ by the sol-gel method with RuO_2 as a cocatalyst showed H_2 generation rate of 4.1 mmol/h·g.[88] It was proposed that both RuO_2 and La in this catalyst acted as electron traps. A molecular cocatalyst—$[Mo_3S_4]^{4+}$—can also improve the photocatalytic property of $NaTaO_3$ with a 28 times enhancement of H_2 generation rate.[89]

3.2 Alkaline Earth Tantalates

3.2.1 Synthetic methodologies of alkaline earth tantalates

The commonly used solid-state reaction method is also applicable for synthesizing alkaline earth tantalates. Specifically, $MgTa_2O_6$ and $BaTa_2O_6$, obtained by solid-state reaction method, showed the hydrogen generation ability by solar water splitting.[38] $BaTa_2O_6$, with an orthorhombic phase, had a good activity, while addition of $Ba(OH)_2$ into the reaction solution and loading of NiO cocatalyst could further improve the hydrogen generation rate.

Comparative investigations of $Sr_2Nb_2O_7$ and $Sr_2Ta_2O_7$ photocatalysts, both of which were synthesized by the solid-state reaction method, with similar layered perovskite structures had been conducted, in which $Sr_2Ta_2O_7$ showed a much higher activity mainly owing to its more negative CB.[90] The relationship between photocatalytic activity and band gap structure had been further investigated by testing the activities of $Sr_2(Ta_{1-X}Nb_X)_2O_7$ tantalates with a series of x values.[91] Still $Sr_2Ta_2O_7$ was the most active one confirming that the CB level was the predominate parameter affecting the activity of solar water splitting. Photoluminescence studies revealed that low efficiency of non-radiative recombination (recombination of photogenerated electrons and holes that does not release photons) of charge carriers also contributed to the high activity of $Sr_2Ta_2O_7$.

$SrTa_2O_6$—not easily obtained by a conventional solid-state reaction—was synthesized by a method using a SrB_2O_4 flux.[92] Upon loading of NiO cocatalyst, such

the $SrTa_2O_6$ photocatalyst had shown a very steady H_2 generation rate of 960 μmol/h·g under UV-light irradiation.

The conventional solid-state reaction method involves high temperature treatment, which will result in the growth of particle size and reduction in surface area. A new polymerizable complex (PC) technique was conducted to synthesize $Sr_2Nb_xTa_{2-x}O_7$ photocatalysts which showed an enhanced activity comparing with those obtained by the solid-state reaction method.[93] The PC system involves the formation a mixed precursor, in which various metal ions (Ta^{5+}, Nb^{5+} and Sr^{2+} in this case) can be uniformly distributed with certain stoichiometric ratio. $Sr_2Ta_2O_7$ synthesized by the PC method at 800 ^oC for 48 h had the highest H_2 and O_2 generation rates of 3517 and 1733 μmol/h·g, respectively. The relatively high surface area owing to the low synthesis temperature and good crystallinity accounted for the high activity.

The highest H_2 generation rate of 7.1 mmol/h·g was detected with NiO loaded $Ba_5Ta_4O_{15}$ among all the alkali earth tantalate photocatalysts.[94] It was claimed that the $Ba_{0.5}TaO_3$ impure phase, as a result of using an excess amount of Ta ions during the PC synthetic process, was responsible for such an excellent activity. The temperature of pyrolysis during such the PC synthetic process would also affect the activity of photocatalysts.[95]

A block copolymer templating method had been conducted to synthesize Mg-Ta mixed oxide with an ordered mesoporous structure and high surface area (123 $m^2 \cdot g^{-1}$), which showed higher activity compared with crystallized $MgTa_2O_6$.[96, 97] In order to maintain the mesoporous structure of Mg-Ta mixed oxide, a lower annealing

temperature was used which may result in a low crystallinity.

Different approaches had been taken to synthesize metastable $Sr_{0.5}TaO_3$ from $H_2Sr_{1.5}Ta_3O_{10}$ that was obtained by the solid-state reaction together with subsequent ion exchange.[98] One approach was the nanosheet processing which involved the exfoliation of $H_2Sr_{1.5}Ta_3O_{10}$ into nanosheets (thickness of ~ 4 nm), stacking and dehydration processes. The other approach was direct dehydration of $H_2Sr_{1.5}Ta_3O_{10}$ by heat treatment. The superior activity of $Sr_{0.5}TaO_3$ obtained by the nanosheet processing approach was due to its larger surface area and existence of large number of stacking faults, which facilitated the formation of defect states in the band gap.

$Sr_2Ta_2O_7$ nanosheets had been synthesized by the hydrothermal method, which showed 70 times higher catalytic activity (H_2 generation rate of 5.2 mmol/h·g and O_2 generation rate of 2.6 mmol/h·g) for solar water splitting comparing with the sample obtained by the solid-solution method.[99] The superior activity of $Sr_2Ta_2O_7$ nanosheets was ascribed to the larger surface area and smaller dimensions which reduced the migration distance of electrons and holes.

Another sol-gel citrate route had been conducted to synthesize a $Ba_5Ta_4O_{15}/Ba_3Ta_5O_{15}$ composite photocatalyst, which had a photocatalytic hydrogen generation rate 1.6 times higher than pure $Ba_5Ta_4O_{15}$.[100] It was proposed that the existence of the $Ba_3Ta_5O_{15}$ phase could enhance the separation of electrons and holes owing to the proper band gap alignment.

3.2.2 Relationship between crystal structures and photocatalytic activities

In addition to the efforts made to improve the synthetic methods for alkaline

earth tantalates, more attention had been paid to understand the relationship between the photocatalytic activities and crystal structures of alkaline earth tantalates. Kudo and coworkers found the activities of the catalysts followed an order of $Sr_2Ta_2O_7$ > $Sr_5Ta_4O_{15}$ > $SrTa_2O_6$ > $Sr_4Ta_2O_9$.[101] $Sr_4Ta_2O_9$ was the least active catalyst mainly due to a low efficiency in electron migration with the narrow CB. Specifically, the electron channel consisted of TaO_6 octahedra were terminated by "insulating" SrO_6 blocks (Fig. 10b). However, for $Sr_2Ta_2O_7$ which had the highest activity, the crystal structure provided an infinite channel for the migration of electrons and holes along the α axis (Fig. 10d). Moreover, the Ta-O-Ta angel of $Sr_2Ta_2O_7$ was close to 180^o since it had the widest CB. In the case of $Sr_5Ta_4O_{15}$, the zigzag-like connection of TaO_6 units (Fig. 10c) was not favorable for the migration of charge carriers. The crystal structure of $SrTa_2O_6$ consisted of edge-sharing TaO_6 units (Fig. 10a) resulted in an even smaller CB.

Layered perovskite alkali earth tantalates with the formula as $ABi_2Ta_2O_9$ (A = Ca, Sr and Ba) had been studied by Chen and coworkers.[102, 103] Specifically, $SrBi_2Ta_2O_9$ was the most active one owing to its suitable crystal and electronic structure.[102] As the lattice distortion was of great importance for the charge separation during the photocatalytic process, orthorhombic $SrBi_2Ta_2O_9$ and $CaBi_2Ta_2O_9$, which had larger lattice distortion, showed higher activity than tetragonal structured $BaBi_2Ta_2O_9$. Additionally, the Ta-O-Ta angel significantly affected the mobility of charge carriers within the catalysts. Ta-O-Ta angel of $SrBi_2Ta_2O_9$ (152.313^o) was closer to 180^o comparing with $CaBi_2Ta_2O_9$ (145.382^o). DFT calculations suggested the addition of

bismuth contribute to the narrowing of the band gap. Further acidic treatment of $SrBi_2Ta_2O_9$ catalyst led to the formation of $H_{1.81}Sr_{0.81}Bi_{0.19}Ta_2O_7$, which showed an enhanced activity with H_2 generation rate of 57.7 mmol/h·g when methanol was used as a sacrificial agent.[103]

3.2.3 Activity enhancement under visible-light irradiation

Another strategy of improving the solar water splitting efficiency of alkaline earth tantalates was to enhance their visible-light responsiveness. Wang and coworkers had synthesized nitrogen doped $Sr_2Ta_2O_7$ with absorption edge red shifted to the visible range.[104] The hydrogen generation rate of $Sr_2Ta_2O_{7-x}N_x$ was nearly two times higher than the undoped one. The quantum efficiencies (calculated in the wavelength region from 280 to 550 nm with an AM1.5 light source) were 4.26% and 2.33% for $Sr_2Ta_2O_{7-x}N_x$ and $Sr_2Ta_2O_7$, respectively. More interestingly, as prepared $Sr_2Ta_2O_{7-x}N_x$ can reduce graphene oxide (GO) into graphene sheets under the irradiation of light. By using Pt loaded GO, a Pt-graphene-$Sr_2Ta_2O_{7-x}N_x$ nanocomposite was synthesized, which appeared to be an effective catalyst for solar water splitting with quantum efficiency of 6.45%. The high activity can be attributed to the high conductivity of graphene, which can effectively transport photo-generated electrons to Pt particles; Pt acted as the H_2 generation center and hindered the recombination of charge carriers. Such combination of nitrogen doping and graphene compositing led to the highly active Pt-graphene-$Sr_2Ta_2O_{7-x}N_x$ photocatalyst.[104] Li and coworkers demonstrated the water reduction and oxidation abilities of $Sr_5Ta_4O_{15-x}N_x$ under visible light irradiation in the presence of a sacrificial agent (e.g.,

$AgNO_3$ and CH_3OH).[105] The extension of the visible light absorption over $Sr_5Ta_4O_{15-x}N_x$ was due to the substitution of nitrogen for oxygen atoms as well as the formation of Ta-N bonds, which resulted in a shift of valance band upward with the mix of N 2p and pre-existing O 2p states. Some other nitrogen-doped tantalum-based layered oxides (e.g., $Ba_5Ta_4O_{15-x}N_x$, $Sr_2Ta_2O_{7-x}N_x$) also showed the ability to utilize visible-light for solar water splitting.

3.3 Other Tantalates

3.3.1 Transition metal tantalates

Considerable efforts have been made to explore other potential tantalates for solar water splitting. Transition metal tantalates, such as $AgTaO_3$, had been investigated by Kudo and coworkers.[106] DFT calculations showed that the VB of $AgTaO_3$ consisted of Ag 4d and O 2p orbitals was more negative than that of the $NaTaO_3$ consisted of O 2p only. Such the VB resulted in a smaller band gap, leading to a red shifted absorption for $AgTaO_3$. $AgTaO_3$ synthesized with an excessive amount of Ag precursor showed higher activity than that prepared in a stoichiometric ratio because of the suppression of silver ion defects. Acidic treatment to remove the metallic Ag particle can further enhance the activity. Guo and coworkers had successfully synthesized $Cd_2Ta_2O_7$ using the sol-gel method, which showed an excellent catalytic activity for solar water splitting.[107] The CB of $Cd_2Ta_2O_7$ was formed by Ta 5d, O 2p and Cd 5s5p orbitals, implying that both Ta and Cd could be the active sites for reaction. Additionally, the increased electron mobility with the

widened CB was responsible for its high activity. $La_{1/3}TaO_3$ with the A-site deficient perovskite-type structure was also active for H_2 generation under UV-light irradiation.[108]

3.3.2 Other main group metal tantalates

Several other main group metal tantalates, including indium tantalates, tin tantalates and bismuth tantalates, had also been investigated.

Indium tantalates for solar water splitting were primarily studied by Zou *et al*.[109] $InTaO_4$ with the monoclinic wolframite-type crystal structure, containing TaO_6 and InO_6 octahedra in a unit cell, showed photocatalytic activity under the visible-light irradiation.[110-113] In order to improve the activity, substitution by 3d-metal ions including Mn, Fe, Co, Ni and Cu, to form $In_{1-x}M_xTaO_4$ (M represents the 3d-metal) was tested.[114, 115] M ions can replace the In sites with silt modifications to lattice parameters. It was found that Ni doped $InTaO_4$ showed the highest activity under both the UV-light irradiation and visible-light irradiation; the quantum yields of the $NiO_x/In_{1-x}Ni_xTaO_4$ photocatalysts were about 0.66% at 402 nm. Notably, such the catalysts were rather stable under visible-light irradiation with the reaction time of 400 h.[116] It was claimed that the loading of NiO_x could effectively enhance the separation of electrons and holes since a short-circuited microphotoelectrochemical cell was built, with the surface of NiO_x as the cathode and surface of $In_{1-x}Ni_xTaO_4$ as the anode. The surface step structure could also account for such the enhanced activity.[117]

Tin tantalates was investigated by Kudo and coworkers. [118, 119] $Sn_2Ta_2O_7$ showed

a good photocatalytic activity for H_2 generation with Pt as the cocatalyst and methanol as the sacrificial agent. It was claimed that the VB of $Sn_2Ta_2O_7$ was formed by Sn 5s orbital, which resulted in a decrease of band gap energy.

Bismuth tantalates were regarded as a group of visible-light responsive photocatalysts. $BiTa_{1-x}Nb_xO_4$ ($0 \leq x \leq 1$) showed two different kinds of crystal structures, triclinic (when x = 0.0 and 0.5) and orthorhombic (when x = 0.2, 0.8 and 1.0), according to Zou's research.[120-122] Orthorhombic $BiTa_{1-x}Nb_xO_4$ had a narrower band gap and a higher activity under UV-light irradiation than the triclinic one. Although $BiTa_{1-x}Nb_xO_4$ had a proper band gap (i.e., 2.3 -2.7 eV), it could not split water under visible-light irradiation mainly because the energy requirement for generating electro-hole pairs was generally higher than the band gap of the semiconductors. Also the photon absorption at the visible range was weak with small amount of charge carriers formed in the bulk. The recombination of electrons and holes resulted in the negligible activity. So other approaches, like dye-sensitizing, had been taken to enhance its visible-light photocatalytic activity. Methylene blue-$BiTaO_4$ was synthesized which showed the potential to generate H_2 by solar water splitting under the visible-light irradiation.[123]

3.4 Tantalates in the PEC System

Limited work on tantalates in the PEC system had been reported, which mainly focused on alkali tantalates. In 1975, Wrighton and coworkers examined photoelectrochemical water splitting properties of $KTaO_3$ and $KTa_{0.77}Nb_{0.23}O_3$.[124]

Confirmed from ^{18}O-enriched water identification, the source of O_2 evaluation was the electrolyte rather than the electrode material. Both of the materials were photo-stable. The negative one-set potentials indicated that reasonable rates of H_2 and O_2 evolution would be expected at zero bias. However, further doping by Ca^{2+} and Ba^{2+} ions did not effectively improve the photo-responsibility of $KTaO_3$.[125]

Another work investigating the behavior of reverse reactions on $NaTaO_3$ and La doped $NaTaO_3$ photoanodes had been done by Unal and coworkers.[126] Doping of La can effectively increase the photocurrent, and loading of NiO can suppress the O_2 photo-reduction reaction. Electrochemical methods had been conducted to synthesize spherical $NaTaO_3$ with a crystalline core and an amorphous shell.[127] Such the $NaTaO_3$ spheres showed an enhanced PEC water splitting activity after a thermal treatment.

The limitation of the fabrication methods for tantalates photoelectrodes in PEC cells is one of major issue hindering their further development. The high quality of connection between tantalates and conductive substrate would bring improvement of the activities. Moreover, to improve the visible-light responsiveness would also be a promising direction.

The research of tantalates has been conducted for decades. However, the efficiencies of tantalate photocatalysts are still far from what are required for the industrial applications. Fortunately, some new benchmarks have been achieved in past several years. The best result shows the hydrogen and oxygen generation rates of 49.6 and 24.6 mmol/h·g, respectively.[78] It is exciting that the data was obtained with pure water as the electrolyte and no cocatalyst was used.

4. Tantalum (oxy)nitrides

Tantalum (oxy)nitrides are promising visible-light responsive catalysts as their band gap energies are relatively small (e.g., ~2.5 eV for TaON, ~2.1 eV for Ta_3N_5 and ~1.9 eV for $BaTaO_2N$) with absorption edges between 500 nm and 660 nm.[21, 128, 129] The hybridization of N 2p with O 2p draws the VBM of tantalum (oxy)nitrides to the negative direction and thus decreases the band gap energy.[17, 19, 130, 131] Moreover, most tantalum (oxy)nitrides have the band gap structure that straddles the redox potentials of H^+/H_2 and O_2/H_2O, indicating that they can potentially realize overall solar water splitting. However, tantalum (oxy)nitrides suffer from the poor stability due to self-oxidation by photogenerated holes; loading cocatalysts could be an effective solution to this issue.

Tantalum (oxy)nitrides can be divided into three categories: TaON, Ta_3N_5 and perovskite-related tantalum oxynitrides.[17] In this section, we will first discuss the development of TaON and Ta_3N_5 in the HPC system, followed by their applications in the PEC system. Recent progress on perovskite-related tantalum oxynitrides is also presented. Relevant work regarding the synthesis and applications of tantalum (oxy)nitrides in both HPC and PEC systems is summarized in Table 3. and Table 4., respectively.

4.1 TaON and Ta_3N_5 in the HPC System

4.1.1 Synthetic methodologies of TaON and Ta_3N_5

High temperature nitridation of Ta_2O_5 precursors is the most common way to

synthesize TaON and Ta_3N_5 photocatalysts. Domen and coworkers are among the first to investigate the photocatalytic water oxidation and reduction properties of TaON and Ta_3N_5.[132-134] Both TaON and Ta_3N_5 were synthesized by high temperature nitridation of Ta_2O_5 powders under a flow of ammonia gas with different flow rates (20 ml/min and 1 l/min for synthesizing TaON and Ta_3N_5, respectively). The absorption edges of TaON and Ta_3N_5 were *ca.* 500 nm and 600 nm corresponding to band gap energies of ~2.5 eV and ~2.1 eV, respectively. Photooxidation of water on Pt loaded TaON and Ta_3N_5 proceeded efficiently with $AgNO_3$ as the sacrificial agent, while the rates of photoreduction reactions were low with methanol as the sacrificial agent. It was proposed that surface imperfection hindered the transportation of photogenerated electrons to the Pt cocatalyst or surface H^+, which resulted in the low HER rate.[133] It is worth pointing out that N_2 can be detected during the activity test, especially at the initial reaction stage. This phenomenon was ascribed to the oxidation of N^{3-} or the adsorbed nitrogen-containing species. However, no N_2 was detected with the further progression of the reaction, indicating that TaON and Ta_3N_5 were essentially stable. Nakato *et al* have further explained how the OER processed on the surface of TaON, which was synthesized by nitridation of commercial Ta_2O_5 powder.[135] Based on *in situ* multiple internal reflection Fourier transform infrared spectroscopy (MIR-IR) experiments, it was claimed that OER occurred on a thin Ta-oxide overlayer as the surface of TaON was slightly oxidized under visible-light irradiation. A surface peroxo species was formed as an intermediate of the reaction. Moreover, a nucleophilic attack of a water molecule on a surface-trapped hole was

proposed to be the initial process.

However, TaON and Ta_3N_5 obtained by the nitridation of commercial Ta_2O_5 powder have relatively large particle sizes and small surface areas, which are unfavorable features for solar water splitting. Much effort had been made to synthesize Ta_2O_5 precursors with advanced properties such as smaller particles size; larger surface area; higher crystallinity and ordered structure.[136-138] Based on a previous study of mesoporous Ta_2O_5,[139] Domen and coworkers had synthesized ordered mesoporous Ta_3N_5 with crystalline thin-wall structure (Fig. 11a); its activity was three times higher than that of bulk Ta_3N_5.[136] The mesoporous Ta_3N_5 had large surface area (100 m^2/g) and small dimensions (pore size of 4 nm and wall thickness of 2 nm). Therefore, the efficient charge transfer of photogenerated electrons and holes to the surface active sites accounted for the excellent activity. The silica coating process by chemical vapor deposition (CVD) of tetramethyl orthosilicate before the high temperature nitridation of mesoporous Ta_2O_5 was important. The deposited silica layer, which was removed afterwards, served as a scaffold against the phase transition during nitridation to maintain the mesoporous structure. Ta_3N_5 nanoparticles with various sizes can be synthesized by using mesoporous carbon nitride (C_3N_4) as the template, which had a controllable pore size (Fig. 11b).[137] Ta_3N_5 with a smaller particle size and a larger surface area showed a one magnitude higher activity than the bulk Ta_3N_5. Such the high activity was resulted from the short diffusion length of charge carriers. This method was further improved by synthesizing an ordered porous graphitic-C_3N_4 (Fig. 11c) template through the polymerization of cyanamide using

close-packed silica nanospheres as a primary template (Scheme 3).[138] Ta_3N_5 photocatalyst obtained by such the method (Fig. 11d) showed an improved activity owing to its ordered structure and increased surface area. Moreover, the decreased nitridation temperature, resulting in a lower extent of defect sites, contributed to the enhancement.

Anther strategy, in addition to improve the quality of Ta_2O_5 precursors, is to improve the nitridation conditions. High pressure ammonothermal treatment had been proved to be a useful way to attain Ta_3N_5 with enhanced HER properties from an aqueous methanol solution under visible-light irradiation.[140] The high pressure ammonothermal treatment can suppress the formation of surface defects and thus enhance the electron transfer from the surface of Ta_3N_5 to the Pt cocatalyst. It was claimed that the density of surface defects was correlated with the background level of UV-visible spectroscopy absorption. Materials with higher density of defects were expected to have a stronger intensity of background absorption at a longer wavelength ($\lambda \geq 600$ nm). Among all the treated Ta_3N_5 powders, the one treated under 50 MPa of NH_3 showed the lowest background UV-visible spectroscopy absorption and the highest photocatalytic activity.

Several other direct synthetic methods have also been explored to attained Ta_3N_5 with high activities. Ta_3N_5 nanoparticles—with the size ranging from 20 nm to 50 nm—had been synthesized by homogeneously chemical reduction of $TaCl_5$ by sodium.[141] The photocatalyst showed a better activity compared to bulk Ta_3N_5 and was stable without deactivation after an 82h reaction.

4.1.2 Bulk/surface modification

Modification by introducing external compositions had been regarded as an effective approach to attain TaON and Ta_3N_5 with enhanced activities. In this part, the modification effects of metal oxide (i.e. ZrO_2), organic dyes and alkaline salts to the TaON and Ta_3N_5 photocatalysts will be discussed.

Modification of TaON with monoclinic ZrO_2 was first investigated by Domen and coworkers.[142-145] The ZrO_2-modified TaON showed an enhanced HER activity under visible-light irradiation with Ru as a cocatalyst comparing with that of either ZrO_2 or TaON. Addition of ZrO_2 could suppress the formation of surface defects, in the form of reduced tantalum species, which were created during the nitridation process.[142] Such the claim was proved by the weaker intensity of UV-visible diffuse reflectance spectra at a longer wavelength ($\lambda \geq 500$ nm) for ZrO_2-modifed TaON photocatalysts. However, excessive loading of ZrO_2 would lead to the coverage of surface active sites on TaON, decreasing the H_2 generation rate. The addition of monoclinic ZrO_2 could also effectively suppress the aggregation of particles when using nanoparticulate Ta_2O_5 (30-50 nm) as the precursor.[143] The resultant $Zr_xTa_{1-x}O_{1+x}N_{1-x}$ photocatalyst showed an enhanced activity with H_2 generation rate of 0.25 mmol/h·g. Additionally, the effect of ZrO_2 precursors (e.g., ZrO_2, $ZrO(NO_3)_2{\cdot}2H_2O$, $ZrOCl_2{\cdot}8H_2O$, $Zr(O\text{-}i\text{-}C_3H_7)_4$ and $ZrCl_4$) on the photocatalytic activity of ZrO_2-TaON had been studied.[144] The $ZrO(NO_3)_2{\cdot}2H_2O$-derived sample with well-dispersed ZrO_2 nanoparticles (particle size of 10-30 nm) showed the highest H_2 generation rate (i.e., 445 ± 35 umol/h·g). The effective contact between ZrO_2 and

TaON in the $ZrO(NO_3)_2 \cdot 2H_2O$-derived sample was considered to suppress the generation of defects during nitridation. Aggregation of ZrO_2 particles in samples prepared with ZrO_2 and $Zr(O\text{-}i\text{-}C_3H_7)_4$ would cover the active sites on the surface of TaON. Chlorine species in $ZrOCl_2 \cdot 8H_2O$-derived and $ZrCl_4$-dervied samples may have a negative effect on the photocatalytic activity. When simultaneously modified with proper cocatalysts (IrO_2, Cr_2O_3 and RuO_x) for water oxidation and reduction, ZrO_2/TaON could achieve overall water splitting without using sacrificial agents, although the activity was low.[145] Cocatalysts played different roles in IrO_2/Cr_2O_3/RuOx/ZrO_2/TaON photocatalyst for the solar water splitting reaction as illustrated in Scheme 4. RuO_x could effectively promote the H_2 generation ability of ZrO_2/TaON by extracting photogenerated electrons from the CB of the TaON. However, no O_2 was detected for the RuO_x/ZrO_2/TaON photocatalyst. Photodeposited Cr_2O_3 helped achieve overall water splitting for the RuO_x/ZrO_2/TaON photocatalyst because Cr_2O_3 modification suppressed the photoreduction of O_2 on RuO_x. Loading of colloidal IrO_2, which acted as water oxidation sites, could effectively improve the stability of $Cr_2O_3/RuO_x/ZrO_2$/TaON photocatalyst as IrO_2 can suppress the self-oxidation of TaON by extracting photogenerated holes out of the bulk of TaON.

Modification effects of porphyrin dyes on the photocatalytic activity of TaON had been investigated. [146] Zn-TPP dimer showed the most positive effect as it could absorb visible light and improve the reduction ability of TaON.

The activity of Ta_3N_5 for photocatalytic O_2 evolution under visible-light demonstrated a 6-fold improvement when the starting martial, Ta_2O_5, was modified by

alkaline salts (Na_2CO_3 in this case which showed the largest enhancement).[147] The addition of Na_2CO_3 introduced the nucleation of $NaTaO_3$ at the initial stage of the nitridation process (Fig. 12a). This phenomenon resulted in the dispersed particles with smaller sizes and improved crystallinity (Fig. 12b, c), which was claimed to be the principal reasons for the activity enhancement.

4.1.3 Z-scheme systems involving TaON and Ta_3N_5

Since TaON and Ta_3N_5 exhibit high photocatalytic activities for HER, they are extensively investigated as H_2 evolution photocatalysts in Z-scheme overall water splitting systems.[142, 148-153]

The first investigation involved Pt-TaON and Pt-WO_3 as the H_2 and O_2 evolution photocatalysts, respectively, together with IO_3^-/I^- as a shuttle redox mediator.[148] The quantum efficiency of this system for overall solar water splitting was *ca.* 0.4% at 420 nm without notable deactivation even after 100 h. The activity was approximately 1.5 times higher when Pt-ZrO_2/TaON was used as the water photoreduction catalyst. Such the high activity attributed to the enhanced HER activity resulting from the lower density of surface defects in ZrO_2/TaON.[142] Effects of different cocatalysts on ZrO_2/TaON, oxygen generation catalysts in Z-scheme, redox mediators and reaction conditions were further investigated.[150] At the optimized circumstance, an apparent quantum yield of 6.3% was achieved at 420.5 nm with stoichiometric H_2 and O_2 generation.

Ta_3N_5—modified with nanoparticulate Ir and rutile TiO_2—can act as an O_2 evolution photocatalyst in a Z-scheme solar water splitting system under visible-light,

with Pt-ZrO_2/TaON as H_2 evolution photocatalyst and IO_3^-/I^- as a shuttle redox mediator.[151] It was claimed that Ir nanoparticles exhibited the ability to reduce IO_3^-, and rutile TiO_2 preferentially absorb IO_3^- and thus hindered the access of I^- which suppressed the backward reaction of I^- oxidization. Ir species at the surface of TiO_2 was the reaction center for the reduction of IO_3^- with electrons "pumped" from Ta_3N_5. OER proceed at the surface of Ta_3N_5 with photogenerated holes.

Another kind of Z-scheme systems with TaON as the sole photocatalytic material, which was used as both H_2 and O_2 evolution photocatalysts, was investigated. Such the system with RuO_2 loaded TaON as the O_2 generation catalyst, and Pt loaded TaON as the H_2 generation catalyst showed relatively low activity.[149] A higher overall efficiency was detected by using Pt loaded ZrO_2/TaON as the H_2 generation catalyst instead.[152] The optimally dispersed RuO_2 nanoparticles on TaON had the abilities to reduce IO_3^- and oxidize water simultaneously. However, the reverse reactions including the oxidization of I^-, reduction of O_2 and self-decomposition on RuO_2/TaON photocatalyst hindered the further development of such systems.

A new Z-scheme solar water splitting system without shuttle redox mediators had been constructed with Ir-CoO_x-Ta_3N_5 as the O_2 generation catalyst and Ru loaded Rh doped $SrTiO_3$ as the H_2 generation catalyst.[153] This system showed high generation rates of H_2 and O_2 mainly owing to the suppression of revers reaction in the absence of redox mediators.

4.1.4 Morphology control of TaON and Ta_3N_5

Tuning the morphologies of TaON and Ta_3N_5 materials was considered to be an

alternative mean to improve their activities for photocatalytic water splitting. Macroporous TaON and Ta_3N_5, exhibiting photonic behavior, were synthesized by using PS spheres as the template (Fig. 13a-d).[154] Samples with macroporous structure were more active comparing with non-porous ones. However, the surface area-normalized activities of non-porous Ta_2O_5 and Ta_3N_5 were higher than those of macroporous samples. In contrast, macroporous TaON showed an enhanced surface area-normalized activity owing to the presence of both γ-TaON and β-TaON phases, which resulted in the promoted electron-hole separation with the existence of the interface.

TaON hollow spheres coupled with Ta_3N_5 quantum dots (QDs) had been synthesized *via* an *in situ* chemical reduction route (Fig 13h-k).[155] A high O_2 generation rate of 208.2 μmol/h and an apparent quantum efficiency of 67% under 420 nm light were detected. The enhanced activity of such the Ta_3N_5 QDs coupled TaON hollow spheres was attributed to the promoted charge carrier separation with the help of heterojunctions as illustrated in Fig. 13l. Also it was very stable owing to the strong interaction between Ta_3N_5 and TaON.

Tantalum (oxy)nitrides with a hierarchical hollow urchin-like spherical nanostructure had been synthesized by an *in situ* self-assembly wet-chemical route together with post thermal nitridation (Fig 13e, f).[156] Metastable single-phase γ-TaON hollow urchin-like spheres, which were obtained during the phase transformation process (illustrated in Fig. 13g), demonstrated an outstanding activity, with H_2 generation rate as high as 381.6 μmol/h and an apparent quantum efficiency of 9.5%

under 420 nm irradiation. Such the good activity was ascribed to its unique structural properties such as a large surface area and a short migration distance for charge carriers. A higher CB of γ-TaON also contributed to the high activity. Moreover, the unique hierarchical hollow urchin-like spherical nanostructure with large specific surface area introduced multiple light reflections within the hollow chamber.

4.2 TaON and Ta_3N_5 in the PEC System

4.2.1 Fabrication methods of TaON and Ta_3N_5 anode materials

TaON and Ta_3N_5 have been investigated as anode materials to conduct solar water splitting in the PEC system. However, fabrication method of photoelectrodes is crucial for the performance of materials in the PEC system. Therefore, different fabrication methods of TaON and Ta_3N_5 photoanodes are investigated.

Domen and coworkers had tested the electrochemical properties of Ta_3N_5 thin films, which was synthesized by high temperature nitridation of a Ta_2O_5 layer formed on a Ta foil. This Ta_3N_5 film showed an anodic current when irradiated with visible-light and applied with a potential bias.[157] However, the Ta_3N_5/Ta electrode was not stable since it suffered from self-oxidation during the reaction, whereas the photocurrent was steady when a solution of $Fe(CN)_6^{3-}$/$Fe(CN)_6^{4-}$ was used. The influence of Ta_3N_5 film thickness on the photoelectrochemical performance had also been investigated.[158] Indeed, thicker films (630 nm and 780 nm) with highly textured surface and porosity exhibited much higher photocurrent comparing with thinner dense films (60 nm and 260 nm). However, the 780 nm film exhibited lower

photocurrent comparing with 630 nm film. This was because photogenerated electrons in 780 nm film had to diffuse a longer distance to the surface, which lowered the efficiency. It was found that the photoelectrochemical performance of such the Ta_3N_5 film could be remarkably improved by thermal or mechanical exfoliation of the surface layer, which was regarded as recombination centers (as illustrated in Fig. 14a).[159] After loading of a $Co(OH)_x$ cocatalyst, the saturated photocurrent showed a great increase for the sample upon surface mechanical exfoliation treatment, while only a slight change was observed for the samples without such treatment (Fig. 14b). This phenomenon suggested that the surface layer hinder the transfer of photogenerated charge carriers. A photocurrent as high as 5.5 mA/cm^2 at 1.23 vs. RHE was detected for the $Co(OH)_x$ loaded Ta_3N_5/Ta photoanode after thermal exfoliation of surface layer.

A porous TaON electrode had been fabricated by spreading a viscous slurry of TaON particles on the fluorine-doped tin oxide (FTO) coated conducting glass.[160] The formation of necks between TaON nanoparticles upon thermal treatment could improve the conduction of charge carriers and increase the photocurrent of TaON anode. However, heat treatment at higher temperature under air could oxidize TaON thus deactivate the material. The TaON electrode upon necking treatment with $TiCl_4$ showed an approximately 30-fold increase of photocurrent because of the established electron transportation channels between TaON particles.

An improved fabrication method by using electrophoretic deposition had been conducted to obtain a porous TaON electrode with a relatively uniform thickness of *ca.*

2 μm on an FTO coated glass.[161] The subsequent $TaCl_5$ necking treatment and loading of IrO_2 cocatalyst can significantly increase the activity and stability of the TaON anode. An incident photon to current efficiency (IPCE) of *ca.* 76% at 400 nm at 0.6 V vs Ag/AgCl was detected. It was claimed that $TaCl_5$ necking treatment first formed Ta_2O_5 bridges between TaON particles by annealing the electrode in air. Then heat treatment under NH_3 atmosphere converted Ta_2O_5 bridges into TaON and further improved the electron transportation within the electrode. It is worth pointing out that overall solar water splitting into H_2 and O_2 was demonstrated with the IrO_2-TaON anode under visible-light irradiation at a potential bias of 0.6-1 V. The IrO_2 cocatalyst could scavenge photogenerated holes, which hindered the deactivation of TaON. This method was also applicable to fabricate IrO_2-loaded Ta_3N_5 photoanode in the PEC system with an IPCE of 31% at 500 nm and at 1.15 vs. RHE.[162]

The electrophoretic deposition had also been used to construct heterojunctions, which is a common approach to enhance the photocatalytic activities of semiconductors. A $CaFe_2O_4$/TaON photoanode had been fabricated, which showed a five-times higher photocurrent density at 1.23 V vs. RHE comparing with pure TaON photoanode.[163] Electrochemical impedance spectroscopy (EIS) studies indicated that the formation of the p-n heterojunctions facilitated the separation of charge carriers and thus increased the photocurrent. The addition of $CaFe_2O_4$ can further enhance the absorption of incident light since it had a band gap of 1.9 eV.

Top-down approaches (a group of techniques that involve the decomposition of a large parent entity, such as physical vapor deposition (PVD), chemical vapor

deposition (CVD), and atomic layer deposition (ALD)) have also been conducted to fabricate TaON and Ta_3N_5 photoanodes. Radio-frequency magnetron sputtering was conducted to deposit Ta_3N_5 films on a Ta substrate.[164] Loading of IrO_2 cocatalyst can further increase the photocurrent and the stability of the Ta_3N_5 anode. DC reactive sputtering was also employed to produce TaO_xN_y/FTO glass photoanode at room temperature without NH_3 post-treatment.[165] By adjusting the pressure of O_2 (P_{O2}) in the sputtering atmosphere, the crystallization, film roughness, oxygen content and band gap energy of the electrode could be tuned. TaO_xN_y/FTO photoanode with the optimal activity was obtained at P_{O2} of 1.9×10^{-4} mbar. Additionally, Mullins and coworkers had successfully synthesized nanostructured Ta_3N_5 films through reactive ballistic deposition at a glancing angle and subsequent nitridation.[166] The deposition angle was important as nanoporous film obtained at $\alpha = 70^o$ exhibited a photocurrent ~3 times higher than that of the dense film obtained at $\alpha = 0^o$. This phenomenon was ascribed to the more open structure of the nanoporous film, which shortened the transport pathway for photogenerated holes to the solid-liquid interface.

4.2.2 Strategies to improve the stability of TaON and Ta_3N_5

As TaON and Ta_3N_5 materials surfer from self-oxidation during the photocatalytic processes, methods to improve their stability have been developed, among which loading of proper cocatalysts is a fairly effective approach.

The TaON photoanode loaded with highly dispersed CoO_x nanoparticles, which effectively scavenge photogenerated holes, showed an enhanced stability comparing with the unloaded sample.[167] Moreover, when a phosphate solution was used as the

electrolyte, an increased photocurrent was detected owing to the formation of cobalt phosphate (Co-Pi) composite phases. By using such the photoanode and electrolyte, the amounts of H_2 and O_2 generated were close to that calculated from the number of electrons passing through the outer circuit. By employing a nanoparticulate Co_3O_4 cocatalyst and a NaOH electrolyte, the stability of Ta_3N_5 photoanode was significantly improved with about 75% of the initial photocurrent remained after 2 h reaction at 1.2 V vs. RHE.[168] The abundant and compact nano-junctions between uniformly distributed Co_3O_4 and Ta_3N_5 were crucial for the improved stability, since the nano-junctions could ensure an efficient transfer of photogenerated holes through the interface.

Loading Co species before the nitridation process had been investigated to synthesize tantalum cobalt nitride, which showed an enhanced visible-light activity and stability.[169] The tantalum cobalt nitride could be regarded as a mixture of Ta_3N_5 and Co_xN_y. It was claimed that the good conductivity of Co_xN_y facilitated electron transfer and suppressed recombination of charge carriers. Oxidized Co_xN_y, in the form of cobalt oxide, could also act as a cocatalyst for the oxidation of water.

4.2.3 Morphology control of TaON and Ta_3N_5 photoanodes

Morphology control is crucial to improve the photocatalytic activity of semiconductors in the solar water splitting. Among all kinds of different morphologies, one dimensional structure is typically desirable since it provided relatively large surface area, sufficient length to absorb incident light and shortened diffusion distance for charge carriers. A large number of studies had been conducted to fabricate TaON

and Ta_3N_5 photoanodes with the one dimensional topologies such as nanotube arrays[170-172], nanowire bundles[173] and nanorod arrays[174-177].

The anodization method has been commonly used to synthesize Ta_2O_5 nanotube arrays on a Ta substrate, which can be converted into TaON and Ta_3N_5 nanotube arrays with the subsequent nitridation. Misra and coworkers first used such the TaON nanotube arrays (Fig. 15a) for H_2 production in the PEC system. which showed much higher photocurrent comparing with other electrodes such as Ti nanotubes/Ti, Fe_2O_3 nanotubes/Fe, and Fe_2O_3 nanoparticles/Fe.[170] Grimes and coworkers had synthesized Ta_3N_5 nanotube arrays (Fig. 15b-e) by anodizing the Ta foil in a concentrated H_2SO_4 and HF mixture.[171] When the 85% of HF was replaced by deionized water, the violent electrochemical reaction, which resulted in the separation of nanotubes from the substrate, was restrained. Owing to the thin-wall structure of Ta_3N_5 nanotube arrays, the nitridation temperature can be decreased to 700 ^oC (850 ^oC was usually used) to fully convert Ta_2O_5 into Ta_3N_5. The synthesized Ta_3N_5 nanotube arrays showed the highest IPCE of 5.3% at 450 nm with a 0.5 V DC bias. Effects of IrO_2, Co_3O_4, Co-Pi and Pt cocatalysts on the photocatalytic properties of Ta_3N_5 nanotube arrays were further studied.[172] Among all these cocatalysts, Pt itself was inefficient to improve the activity of Ta_3N_5 nanotube arrays. The faradaic efficiency of the Co_3O_4-loaded sample was as high as 88% measured by scanning electrochemical microscopy. Moreover, Co_3O_4 and Co-Pi cocatalyst can improve the stability of Ta_3N_5 nanotube arrays.

Single-crystalline Ta_3N_5 nanowire bundles (Fig. 15c) had been synthesized *via* a two-step method. $K_6Ta_{10.8}O_{30}$ micro/nanowires was first obtained by a molten salt

method, and the following nitridation converted it into Ta_3N_5.[173] The appropriate ramp rate of temperature (i.e., 2 ^oC/min) during the nitridation was critical to maintain the structure of nanowire bundles. Upon loading of an IrO_2 cocatalyst, such the Ta_3N_5 nanowire bundles showed enhanced PEC performance and stability comparing with Ta_3N_5 powder.

Ta_3N_5 nanorods had also been widely investigated because of their unique structures and high activities. A template-free synthetic method, involving a vapor-phase hydrothermal process and a subsequent nitridation, was performed to attain Ta_3N_5 nanorod arrays on a Ta foil (Fig 16a).[177] When modified with a $Co(OH)_x$ cocatalyst, such the Ta_3N_5 nanorod arrays showed a stable photocurrent of 2.8 mA/cm^2 and IPCE of 37.8% (480 nm) at 1.23 V vs. RHE. The unique nanorod structure provided more surface reaction sites with the large surface area. Moreover, the small radial dimension of nanorod resulted in effective charge separation/migration, while the large longitudinal dimension kept the sufficient absorption of incident light. A similar approach had also been employed by Zhu and coworkers to synthesize Ta_3N_5 nanorod arrays (Fig. 16b).[174] The time-dependent experiments showed that Ta_2O_5 nanoparticles (less than 100 nm) were first formed, together with some short nanorods. After 3 h, uniformly aligned Ta_2O_5 nanorod arrays were obtained. However, further growth resulted in the formation of hierarchical chrysanthemum-like Ta_2O_5 arrays. The Ta_3N_5 photoanode obtained by nitridation of the uniformly aligned Ta_2O_5 nanorod arrays showed the highest photocurrent among all the nitrided anodes. Further modification with a Co_3O_4-$Co(OH)_2$ bilayer cocatalyst

could not only enhance the photoelectrochemical performance but also improve the stability of Ta_3N_5 nanorod arrays. This was mainly ascribed to the uniform loading of cocatalysts and fast specific charge transfer kinetics as had been demonstrated by EIS.

Domen and coworkers had developed a scalable through-mask anodization method to synthesize vertically aligned Ta_2O_5 nanorod arrays, which was converted into Ta_3N_5 with nitridation.[175] In this process, porous anodic alumina (PAA) was first fabricated on the surface of Ta foil by anodization of an Al coated Ta foil in an oxalic acid solution (illustrated as step a and b in Fig 16d). Ta_2O_5 nanorods, which embedded into the nanochannels of PAA, were synthesized by anodizing the Ta foil through the PAA mask (step c in Fig 16d). Removal of the PAA mask and nitridation resulted in the formation of Ta_3N_5 nanorod arrays (step d and e in Fig 16d). The film of Ta_2O_5 nanorod arrays obtained by this method showed great toughness, which enabled the increase of nitridation temperature to be as high as 1000 ^oC. Consequently, metallic Ta_5N_6 and Ta_2N interlayer with good conductivity was formed, while only polycrystalline Ta_3N_5 interlayer was obtained at nitridation temperature of 850 ^oC. Such the high conductive interlayer could facilitate the migration of photogenerated electrons to the cathode. Moreover, the high temperature nitridation could improve the crystallinity of Ta_3N_5. Both factors accounted for the high activity of Ta_3N_5 nanorod arrays loaded with IrO_2 cocatalyst. It was claimed that the fine nanorod morphology (Fig. 16d, e) can decouple the light absorption length from the minority carrier diffusion length which make sure of the efficient light absorption as well as shorter distance of migration for holes to the surface. Also the large surface area of nanorod

structure could provide more surface reaction sites, enhance light absorption and reduce reflection. Doping of barium into such the nanorod arrays could further enhance the activity.[176] The obtained Co-Pi/Ba-Ta_3N_5 nanorod photoanode showed a solar energy conversion efficiency of 1.5% with stable production of stoichiometric oxygen and hydrogen. The Faraday efficiencies of the OER and HER are 96% and 98%, respectively. It was claimed that Ba doping could suppress the formation of Ta_5N_6 phase, which was less conductive than Ta_2N, to further enhance the conductivity of the interlayer. Additionally, considering surface hydroxyl concentration of Ta_3N_5 nanorod could be increased as a result of Ba doping, the flat band potential of Ba-Ta_3N_5 showed a cathodic shift comparing with undoped sample which was the reason for the shift of one-set potential and the enhanced activity.

4.3 Perovskite-related Tantalum Oxynitrides

4.3.1 Synthetic methodologies of perovskite-related tantalum oxynitrides

$LaTaON_2$ and $ATaO_2N$ (A = Ca, Sr and Ba) with perovskite-like structures, synthesized by high temperature nitridation of relevant tantalates, have been investigated as the photocatalysts for solar water splitting in the HPC system.[128, 129, 178] For $LaTaON_2$, a Pt/Ru cocatalyst was demonstrated to be more effective than either Pt or Ru.[178] However, these materials only showed the ability to reduce H^+ into H_2 at the presence of sacrificial electron donors owing to the insufficient overpotential of VB for the oxidation of water.[129] Therefore, Pt-$ATaO_2N$ (A = Ca, Sr and Ba) had been studied as a H_2 evolution photocatalyst in a two-step water splitting system with

Pt-WO_3 as the O_2 evolution photocatalyst and IO_3^-/I^- as a shuttle mediator.[179, 180] It was found that both Pt-$CaTaO_2N$ and Pt-$BaTaO_2N$, in combination with Pt-WO_3, achieved overall solar water splitting with the utilization of visible-light. However, Pt-$SrTaO_2N$ was unable to stably produce H_2 because of the photo-induced self-oxidative decomposition, which had been proved by the release of N_2 in the presence of I^-.

$CaTaO_2N$ had been synthesized with different precursors which were layered metal oxide (e.g., $RbCa_2Ta_3O_{10}$ or $HCa_2Ta_3O_{10}$) and bulk-type Ca-Ta oxide obtained by PC method.[181] It was demonstrated that $CaTaO_2N$ synthesized from layer metal oxide showed higher activity towards H_2 generation under visible-light irradiation owing to its less-aggregated morphology, larger band gap and lower density of anionic defects.

$[Ca_2Ta_3O_{9.7}N_{0.2}]^-$ nanosheet was synthesized by exfoliating a layered perovskite oxynitride ($CsCa_2Ta_3O_{9.7}N_{0.2}$).[182] Monolayer nanosheet, together with some bilayer and trilayer samples, showed much higher activity comparing with the parent layered oxynitride owing its large surface area, thick structure (approximate 2.8-3.1 nm) and high crystallinity. When loaded with Rh cocatalyst, such the nanosheets exhibited the ability to split pure water into H_2 and O_2 under UV-light irradiation.

4.3.2 Perovskite-related tantalum oxynitrides solid solutions

The $BaZrO_3$-$BaTaO_2N$ solid solution with a perovskite structure showed much higher activity comparing with $BaTaON_2$ itself in the HPC system.[183] Such the enhancement was ascribed to the enlarged band gap and reduced defect density by the

addition of $BaZrO_3$. The enlarged band gap could increase the driving force for OER and HER, and the reduced defect density can effectively suppress the recombination of photogenerated electrons and holes. The activity decreased when an excess amount of $BaZrO_3$ was added because of the decrease in crystallinity. Since $BaZrO_3$-$BaTaO_2N$ exhibit outstanding ability to absorb visible-light (with absorption edge extended to 660 nm), it could be a promising candidate in the PEC system. Upon post necking treatment with $TiCl_4$ and loading of IrO_2 cocatalyst, $BaZrO_3$-$BaTaO_2N$ electrode showed the ability to produce stoichiometric H_2 and O_2 from water with an external bias of 1.0 V vs. Pt cathode.[184] It was inspiring since semiconductors with such small band gap could be capable of both photocatalytic reducing and oxidizing of water.

$Na_xLa_{1-x}TaO_{1+2x}N_{2-2x}$ (x = 0.1, 0.2, 0.25, 0.3, 0.5, 0.75 and 0.85) solid solutions with different band gap structures had been synthesized by nitridation of amorphous oxide precursors.[185] It was found that $Na_xLa_{1-x}TaO_{1+2x}N_{2-2x}$ (x = 0.20-0.85) achieved O_2 evolution owing to the appropriate band gap structure.

The development of tantalum (oxy)nitride photocatalysts is very fast in recent years, particularly in PEC systems; they are among the most promising tantalum-based semiconductors. The highest photocurrent of 6.7 mA/cm^2 at 1.23 V vs. RHE has been obtained for a Co-Pi/Ba-Ta_3N_5 nanorod photoanode.[159] The improvement of the photoelectrode fabrication methods and the controlling of fine morphologies are important directions for the enhanced performance. However, the poor stability of tantalum (oxy)nitrides is still an serious issue which, hinders their further applicable utilization.

5. Concluding Remarks and Outlooks

Both HPC and PEC systems are frequently examined for solar water splitting process, which have intrinsic advantages and disadvantages. The HPC system is relatively simple and more suitable to be scaled up for industrial applications. However, such the system comes across the difficulties to separate H_2 from O_2 and to prevent the back reaction. These problems will lead to safety issues and lower efficiencies. The separation of generated H_2 and O_2 is much easier in the PEC system, since they are obtained individually on the cathode and anode, respectively. Moreover, the possibility to add external bias enlarges the scope to choose photocatalytic semiconductor materials. However, the configuration in the PEC system is much more complicated.

Most research regarding Ta_2O_5 and tantalates is conducted in the HPC system as they are usually synthesized in the powder form, whereas both the HPC and PEC systems are applied to study the photocatalytic properties of Ta_3N_5. When Ta_3N_5 was studied in the PEC system, the fabrication method of photoelectrode is crucial.

Ta_2O_5 and tantalates have a large band gaps which make them potentially capable to realize overall solar water splitting. Research on Ta_2O_5 and tantalates concentrates on the development of different synthetic methods to improve the photocatalytic activities. However, improving their visible-light responsiveness is urgent. Doping, heterojunctions constructing, and dye sensitizing have been proven to be useful means to achieve this goal. Combination of these approaches may be a promising direction to extend the absorption edge of Ta_2O_5 and tantalates to a further

range. Making use of photonic crystal structures is an alternative way to realize visible-light absorption. As the layered structure of tantalate is crucial for its photocatalytic activities, fine tuning of such structure is of great importance.

It has been widely accepted that the target of the theoretical solar energy conversion efficiency is above 10%.[186] Therefore, photocatalysts or photoelectrodes with sufficient absorption (with absorption edge larger than 600 nm) are needed. Tantalum (oxy)nitrides, especially TaON and Ta_3N_5, are regarded as the most promising candidates among all the tantalum-based semiconductors for solar water splitting owing to their visible-light responsiveness. The theoretical efficiency of TaON and Ta_3N_5 are calculated to be as high as 9.3% and 15.9% under an AM1.5 illumination, respectively.[187] Although TaON and Ta_3N_5 show outstanding activities, more attention should still be paid to further improve their performance in some aspects:

i) Photostability of tantalum (oxy)nitrides. It has been proved that cobalt oxides and Co-Pi are useful cocatalysts to suppress the self-oxidation of TaON and Ta_3N_5.[167, 168, 175] However, other approaches, other than integrating of cocatalysts, are worth trying. For instance, deposition of a thin p-type semiconductor layer which could establish p-n junction at the surface. The established electric field could help the migration of holes out of bulk to the solid-liquid interface, which may potentially hinder the self-oxidation of Ta_3N_5.

ii) Controllable synthetic methods. Since the most common way to synthesize TaON and Ta_3N_5 is high temperature nitridation, phase impurity may be brought in

with inappropriate setting of parameters in this process, especially for TaON. Moreover, synthetic methods should be easy, environmental benign and applicable for scale-up, so it can be used in practice.

iii) Morphology control. The main purpose of morphology control is to shorten the migration distance of charge carriers, improving the conductivity and light absorption ability of photocatalysts. Although one-dimensional-structured TaON and Ta_3N_5 have shown their advantages for solar water splitting,[170-177] innovative design and tuning of the morphologies may also hold the promises to further enhance the activities.

For all the tantalum-based semiconductors, insights of the reaction mechanism and local reaction environment at the solid-liquid interface are worth further investigation. Combination of rational experiment design, advanced characterization techniques such as environmental electron microcopies and *in situ* spectroscopies, and theoretical studies such as DFT calculation could provide useful and strong evidence. Facet tuning and crystal structure control can open up a new way to study the reaction mechanism. Synthesizing photocatalysts with advanced nanostructures can also be a promising direction. Moreover, design and assembly of multifunctional setups for solar water splitting are meaningful for the scale up applications.

The recent developed tantalum-based photocatalysts are still far from large-scale applications from the perspectives of their efficiency and stability. However, as theoretical study and in-depth research have been conducted for semiconductor-based solar water splitting, it is our hope that a new era of solar energy utilization would

come soon.

Acknowledgements

We acknowledge the National Natural Science Foundation of China (21222604), the Program for New Century Excellent Talents in University (NCET-10-0611), the Scientific Research Foundation for the Returned Overseas Chinese Scholars (MoE), and the Program of Introducing Talents of Discipline to Universities (B06006) for financial support.

References

1. M. G. Walter, E. L. Warren, J. R. McKone, S. W. Boettcher, Q. Mi, E. A. Santori and N. S. Lewis, *Chem. Rev.* , 2010, **110**, 6446-6473.
2. R. Agrawal, M. Offutt and M. P. Ramage, *AlChE J.* , 2005, **51**, 1582-1589.
3. A. Fujishima and K. Honda, *Nature*, 1972, **238**, 37-38.
4. A. Kudo and Y. Miseki, *Chem. Soc. Rev.* , 2009, **38**, 253-278.
5. X. Chen, S. Shen, L. Guo and S. S. Mao, *Chem. Rev.* , 2010, **110**, 6503-6570.
6. F. E. Osterloh and B. A. Parkinson, *MRS Bull.* , 2011, **36**, 17-22.
7. X. Chen and S. S. Mao, *Chem. Rev.* , 2007, **107**, 2891-2959.
8. F. E. Osterloh, *Chem. Soc. Rev.* , 2013, **42**, 2294-2320.
9. Y. Lin, G. Yuan, S. Sheehan, S. Zhou and D. Wang, *Energy Environ. Sci.* , 2011, **4**, 4862-4869.
10. S. D. Tilley, M. Cornuz, K. Sivula and M. Grätzel, *Angew. Chem. Int. Ed.* , 2010, **49**, 6405-6408.
11. A. Kudo, *MRS Bull.* , 2011, **36**, 32-38.
12. J. Yang, D. Wang, H. Han and C. Li, *Acc. Chem. Res.* , 2013, **46**, 1900-1909.
13. H. G. Park and J. K. Holt, *Energy Environ. Sci.* , 2010, **3**, 1028.
14. Á. Valdé s, J. Brillet, M. Grätzel, H. Gudmundsdóttir, H. A. Hansen, H. Jónsson, P. Klüpfel, G. Kroes, F. Le Formal, I. C. Man, R. S. Martins, J. K. Nørskov, J. Rossmeisl, K. Sivula, A. Vojvodic and M. Zäch, *Phys. Chem. Chem. Phys.* , 2012, **14**, 49-70.
15. J. Xing, W. Q. Fang, H. J. Zhao and H. G. Yang, *Chem. Asian J.* , 2012, **7**, 642-657.
16. F. E. Osterloh, *Chem. Mater.* , 2007, **20**, 35-54.
17. Y. Moriya, T. Takata and K. Domen, *Coord. Chem. Rev.* , 2013, **257**, 1957-1969.
18. Z. Li, W. Luo, M. Zhang, J. Feng and Z. Zou, *Energy Environ. Sci.* , 2013, **6**, 347-370.
19. K. Maeda and K. Domen, *J. Phys. Chem. C*, 2007, **111**, 7851-7861.
20. C. Chaneliere, J. L. Autran, R. A. B. Devine and B. Balland, *Mat. Sci. Eng. R-Rep.*, 1998, **22**, 269-322.
21. W. Chun, A. Ishikawa, H. Fujisawa, T. Takata, J. N. Kondo, M. Hara, M. Kawai, Y. Matsumoto and K. Domen, *J. Phys. Chem. B*, 2003, **107**, 1798-1803.
22. K. Sayama and H. Arakawa, *J. Photochem. Photobiol., A*, 1994, **77**, 243-247.
23. H. Kominami, M. Miyakawa, S. Murakami, T. Yasuda, M. Kohno, S. Onoue, Y. Kera and B. Ohtani, *Phys. Chem. Chem. Phys.* , 2001, **3**, 2697-2703.
24. Y. Takahara, J. N. Kondo, T. Takata, D. Lu and K. Domen, *Chem. Mater.* , 2001, **13**, 1194-1199.
25. T. Sreethawong, S. Ngamsinlapasathian, Y. Suzuki and S. Yoshikawa, *J. Mol. Catal. A: Chem.* , 2005, **235**, 1-11.
26. Y. Noda, B. Lee, K. Domen and J. N. Kondo, *Chem. Mater.* , 2008, **20**, 5361-5367.
27. J. Zou, C. Liu and Y. Zhang, *Langmuir*, 2006, **22**, 2334-2339.
28. B. Zielińska, E. Mijowska and R. J. Kalenczuk, *Mater. Charact.* , 2012, **68**, 71-76.
29. R. V. Gonçalves, P. Migowski, H. Wender, D. Eberhardt, D. E. Weibel, F. C. Sonaglio, M. J. M. Zapata, J. Dupont, A. F. Feil and S. R. Teixeira, *J. Phys. Chem. C*, 2012, **116**, 14022-14030.
30. J. Huang, R. Ma, Y. Ebina, K. Fukuda, K. Takada and T. Sasaki, *Chem. Mater.* , 2010, **22**, 2582-2587.

31. S. Lin, L. Shi, H. Yoshida, M. Li and X. Zou, *J. Solid State Chem.* , 2013, **199**, 15-20.
32. D. Jing and L. Guo, *J. Phys. Chem. Solids* 2007, **68**, 2363-2369.
33. L. Xu, J. Guan, L. Gao and Z. Sun, *Catal. Commun.* , 2011, **12**, 548-552.
34. L. Xu, J. Guan, W. Shi and L. Liu, *J. Colloid Interface Sci.* , 2012, **377**, 160-168.
35. L. Xu, J. Guan and W. Shi, *ChemCatChem* 2012, **4**, 1353-1359.
36. L. Xu, W. Shi and J. Guan, *Catal. Commun.* , 2012, **25**, 54-58.
37. K. Sayama, H. Arakawa and K. Domen, *Catal. Today* 1996, **28**, 175-182.
38. H. Kato and A. Kudo, *Chem. Phys. Lett.* , 1998, **295**, 487-492.
39. H. Kato and A. Kudo, *Catal. Lett.* , 1999, **58**, 153-155.
40. H. Kato and A. Kudo, *J. Phys. Chem. B*, 2001, **105**, 4285-4292.
41. H. Kato and A. Kudo, *Catal. Today* 2003, **78**, 561-569.
42. Y. Lee, T. Watanabe, T. Takata, M. Hara, M. Yoshimura and K. Domen, *Bull. Chem. Soc. Jpn.* , 2007, **80**, 423-428.
43. J. W. Liu, G. Chen, Z. H. Li and Z. G. Zhang, *Int. J. Hydrogen Energy* 2007, **32**, 2269-2272.
44. J. Shi, G. Liu, N. Wang and C. Li, *J. Mater. Chem.* , 2012, **22**, 18808-18813.
45. A. Ratnamala, G. Suresh, V. D. Kumari and M. Subrahmanyam, *Mater. Chem. Phys.* , 2008, **110**, 176-179.
46. T. Yokoi, J. Sakuma, K. Maeda, K. Domen, T. Tatsumi and J. N. Kondo, *Phys. Chem. Chem. Phys.* , 2011, **13**, 2563-2570.
47. S. Ikeda, M. Fubuki, Y. K. Takahara and M. Matsumura, *Appl. Catal., A*, 2006, **300**, 186-190.
48. H. Tüysüz and C. K. Chan, *Nano Energy*, 2013, **2**, 116-123.
49. T. Ishihara, N. S. Baik, N. Ono, H. Nishiguchi and Y. Takita, *J. Photochem. Photobiol., A*, 2004, **167**, 149-157.
50. C. Hu and H. Teng, *Appl. Catal., A*, 2007, **331**, 44-50.
51. C. Hu, C. Tsai and H. Teng, *J. Am. Ceram. Soc.* , 2009, **92**, 460-466.
52. A. Kudo and H. Kato, *Chem. Lett.* , 1997, **26**, 867-868.
53. T. Kurihara, H. Okutomi, Y. Miseki, H. Kato and A. Kudo, *Chem. Lett.* , 2006, **35**, 274-275.
54. N. Yamatani, V. Petrykin, Y. Matsumoto, K. Tomita, A. Kudo and M. Kakihana, *J. Ceram. Soc. Jpn.* , 2009, **117**, 308-312.
55. A. Kudo, H. Okutomi and H. Kato, *Chem. Lett.* , 2000, **29**, 1212-1213.
56. M. Tian, W. Shangguan, J. Yuan, L. Jiang, M. Chen, J. Shi, Z. Ouyang and S. Wang, *Appl. Catal., A*, 2006, **309**, 76-84.
57. M. Machida, J. Yabunaka and T. Kijima, *Chem. Commun.* , 1999, 1939-1940.
58. M. Machida, J. Yabunaka and T. Kijima, *Chem. Mater.* , 2000, **12**, 812-817.
59. M. Machida, J. Yabunaka, T. Kijima, S. Matsushima and M. Arai, *Int. J. Inorg. Mater.* , 2001, **3**, 545-550.
60. M. Machida, K. Miyazaki, S. Matsushima and M. Arai, *J. Mater. Chem.* , 2003, **13**, 1433-1437.
61. K. Shimizu, Y. Tsuji, M. Kawakami, K. Toda, T. Kodama, M. Sato and Y. Kitayama, *Chem. Lett.* , 2002, **31**, 1158-1159.
62. K. Shimizu, Y. Tsuji, T. Hatamachi, K. Toda, T. Kodama, M. Sato and Y. Kitayama, *Phys. Chem. Chem. Phys.* , 2004, **6**, 1064-1069.
63. K. Shimizu, S. Itoh, T. Hatamachi, T. Kodama, M. Sato and K. Toda, *Chem. Mater.* , 2005, **17**, 5161-5166.

64. M. Machida, T. Mitsuyama, K. Ikeue, S. Matsushima and M. Arai, *J. Phys. Chem. B*, 2005, **109**, 7801-7806.
65. T. Mitsuyama, A. Tsutsumi, T. Hata, K. Ikeue and M. Machida, *Bull. Chem. Soc. Jpn.* , 2008, **81**, 401-406.
66. T. Mitsuyama, A. Tsutsumi, S. Sato, K. Ikeue and M. Machida, *J. Solid State Chem.* , 2008, **181**, 1419-1424.
67. K. Ikeue, T. Mitsuyama, K. Arayama, A. Tsutsumi and M. Machida, *J. Ceram. Soc. Jpn.* , 2009, **117**, 1161-1165.
68. T. Ishihara, H. Nishiguchi, K. Fukamachi and Y. Takita, *J. Phys. Chem. B*, 1998, **103**, 1-3.
69. C. Mitsui, H. Nishiguchi, K. Fukamachi, T. Ishihara and Y. Takita, *Chem. Lett.* , 1999, **28**, 1327-1328.
70. A. Kudo and H. Kato, *Chem. Phys. Lett.* , 2000, **331**, 373-377.
71. A. Yamakata, T. Ishibashi, H. Kato, A. Kudo and H. Onishi, *J. Phys. Chem. B*, 2003, **107**, 14383-14387.
72. H. Kato, K. Asakura and A. Kudo, *J. Am. Chem. Soc.* , 2003, **125**, 3082-3089.
73. H. Husin, H. Chen, W. Su, C. Pan, W. Chuang, H. Sheu and B. Hwang, *Appl. Catal., B*, 2011, **102**, 343-351.
74. H. Husin, W. Su, H. Chen, C. Pan, S. Chang, J. Rick, W. Chuang, H. Sheu and B. Hwang, *Green Chem.* , 2011, **13**, 1745-1754.
75. A. Iwase, H. Kato, H. Okutomi and A. Kudo, *Chem. Lett.* , 2004, **33**, 1260-1261.
76. A. Iwase, H. Kato and A. Kudo, *ChemSusChem* 2009, **2**, 873-877.
77. M. Maruyama, A. Iwase, H. Kato, A. Kudo and H. Onishi, *J. Phys. Chem. C*, 2009, **113**, 13918-13923.
78. J. Sun, G. Chen, Y. Li, R. Jin, Q. Wang and J. Pei, *Energy Environ. Sci.* , 2011, **4**, 4052-4060.
79. H. Hagiwara, N. Ono, T. Inoue, H. Matsumoto and T. Ishihara, *Angew. Chem. Int. Ed.* , 2006, **45**, 1420-1422.
80. M. Nagatomo, H. Hagiwara, S. Ida and T. Ishihara, *Electrochemistry*, 2011, **79**, 779-782.
81. L. Xu, C. Li, W. Shi, J. Guan and Z. Sun, *J. Mol. Catal. A: Chem.* , 2012, **360**, 42-47.
82. A. Iwase, K. Saito and A. Kudo, *Bull. Chem. Soc. Jpn.* , 2009, **82**, 514-518.
83. Z. Li, Y. Wang, J. Liu, G. Chen, Y. Li and C. Zhou, *Int. J. Hydrogen Energy* 2009, **34**, 147-152.
84. W. Chen, C. Li, H. Gao, J. Yuan, W. Shangguan, J. Su and Y. Sun, *Int. J. Hydrogen Energy* 2012, **37**, 12846-12851.
85. X. Zong, C. Sun, Z. Chen, A. Mukherji, H. Wu, J. Zou, S. C. Smith, G. Q. Lu and L. Wang, *Chem. Commun.* , 2011, **47**, 6293-6295.
86. A. Iwase, H. Kato and A. Kudo, *Catal. Lett.* , 2006, **108**, 7-10.
87. A. Iwase, H. Kato and A. Kudo, *Appl. Catal., B*, 2013, **136–137**, 89-93.
88. L. M. Torres-Martínez, R. Gómez, O. Vázquez-Cuchillo, I. Juárez-Ramírez, A. Cruz-López and F. J. Alejandre-Sandoval, *Catal. Commun.* , 2010, **12**, 268-272.
89. S. W. Seo, S. Park, H.-Y. Jeong, S. H. Kim, U. Sim, C. W. Lee, K. T. Nam and K. S. Hong, *Chem. Commun.* , 2012, **48**, 10452-10454.
90. A. Kudo, H. Kato and S. Nakagawa, *J. Phys. Chem. B*, 2000, **104**, 571-575.
91. H. Kato and A. Kudo, *J. Photochem. Photobiol., A*, 2001, **145**, 129-133.
92. H. Kato and A. Kudo, *Chem. Lett.* , 1999, **28**, 1207-1208.

93. M. Yoshino, M. Kakihana, W. S. Cho, H. Kato and A. Kudo, *Chem. Mater.* , 2002, **14**, 3369-3376.
94. H. Otsuka, K. Kim, A. Kouzu, I. Takimoto, H. Fujimori, Y. Sakata, H. Imamura, T. Matsumoto and K. Toda, *Chem. Lett.* , 2005, **34**, 822-823.
95. Y. Sakata, T. Kamigouchi, S. Tanaka, H. Kamioka, K. Matsumoto, H. Fujimori, H. Imamura and J. N. Kondo, *Catal. Sci. Tech.*, 2013, **3**, 1691-1693.
96. M. Uchida, J. N. Kondo, D. Lu and K. Domen, *Chem. Lett.* , 2002, **31**, 498-499.
97. J. N. Kondo, M. Uchida, K. Nakajima, L. Daling, M. Hara and K. Domen, *Chem. Mater.* , 2004, **16**, 4304-4310.
98. K. Inaba, S. Suzuki, Y. Noguchi, M. Miyayama, K. Toda and M. Sato, *Eur. J. Inorg. Chem.* , 2008, **2008**, 5471-5475.
99. C. Zhou, G. Chen, Y. Li, H. Zhang and J. Pei, *Int. J. Hydrogen Energy* 2009, **34**, 2113-2120.
100. R. Marschall, J. Soldat and M. Wark, *Photochem. Photobiol. Sci.*, 2013, **12**, 671-677.
101. K. Yoshioka, V. Petrykin, M. Kakihana, H. Kato and A. Kudo, *J. Catal.* , 2005, **232**, 102-107.
102. Y. Li, G. Chen, H. Zhang, Z. Li and J. Sun, *J. Solid State Chem.* , 2008, **181**, 2653-2659.
103. Y. Li, G. Chen, C. Zhou and Z. Li, *Catal. Lett.* , 2008, **123**, 80-83.
104. A. Mukherji, B. Seger, G. Q. Lu and L. Wang, *ACS Nano*, 2011, **5**, 3483-3492.
105. S. Chen, J. Yang, C. Ding, R. Li, S. Jin, D. Wang, H. Han, F. Zhang and C. Li, *J. Mater. Chem. A*, 2013, **1**, 5651-5659.
106. H. Kato, H. Kobayashi and A. Kudo, *J. Phys. Chem. B*, 2002, **106**, 12441-12447.
107. H. Yang, X. Liu, Z. Zhou and L. Guo, *Catal. Commun.* , 2013, **31**, 71-75.
108. D. Li, J. Zheng, Z. Li, X. Fan, L. Liu and Z. Zou, *Int. J. Photoenergy* 2007, **2007**, 1-7.
109. Z. Zou and H. Arakawa, *J. Photochem. Photobiol., A*, 2003, **158**, 145-162.
110. Z. Zou, J. Ye and H. Arakawa, *Chem. Phys. Lett.* , 2000, **332**, 271-277.
111. Z. Zou, J. Ye and H. Arakawa, *Mater. Res. Bull.* , 2001, **36**, 1185-1193.
112. M. Oshikiri, M. Boero, J. Ye, Z. Zou and G. Kido, *J. Chem. Phys.*, 2002, **117**, 7313.
113. J. Ye, Z. Zou, H. Arakawa, M. Oshikiri, M. Shimoda, A. Matsushita and T. Shishido, *J. Photochem. Photobiol., A*, 2002, **148**, 79-83.
114. Z. Zou, J. Ye and H. Arakawa, *Catal. Lett.* , 2001, **75**, 209-213.
115. Z. Zou, J. Ye, K. Sayama and H. Arakawa, *J. Photochem. Photobiol., A*, 2002, **148**, 65-69.
116. Z. Zou, J. Ye, K. Sayama and H. Arakawa, *Nature*, 2001, **414**, 625-627.
117. Z. Zou, J. Ye and H. Arakawa, *J. Phys. Chem. B*, 2002, **106**, 13098-13101.
118. Y. Hosogi, K. Tanabe, H. Kato, H. Kobayashi and A. Kudo, *Chem. Lett.* , 2004, **33**, 28-29.
119. Y. Hosogi, Y. Shimodaira, H. Kato, H. Kobayashi and A. Kudo, *Chem. Mater.* , 2008, **20**, 1299-1307.
120. Z. Zou, J. Ye and H. Arakawa, *Solid State Commun.* , 2001, **119**, 471-475.
121. Z. Zou, J. Ye, K. Sayama and H. Arakawa, *Chem. Phys. Lett.* , 2001, **343**, 303-308.
122. Z. Zou, H. Arakawa and J. Ye, *J. Mater. Res.* , 2002, **17**, 1446-1454.
123. D. L. S. Maia, I. Pepe, A. F. da Silva and L. A. Silva, *J. Photochem. Photobiol., A*, 2012, **243**, 61-64.
124. A. B. Ellis, S. W. Kaiser and M. S. Wrighton, *J. Phys. Chem.*, 1976, **80**, 1325-1328.
125. I. E. Paulauskas, J. E. Katz, G. E. Jellison, N. S. Lewis, L. A. Boatner and G. M. Brown, *J. Electrochem. Soc.* , 2009, **156**, B580-B587.
126. Y. Matsumoto, U. Unal, N. Tanaka, A. Kudo and H. Kato, *J. Solid State Chem.* , 2004, **177**,

4205-4212.

127. X. Wang and L. I. Zhou, *Nano*, 2013, **08**, 1350024.
128. G. Hitoki, T. Takata, J. N. Kondo, M. Hara, H. Kobayashi and K. Domen, *Electrochemistry*, 2002, **70**, 3.
129. D. Yamasita, T. Takata, M. Hara, J. N. Kondo and K. Domen, *Solid State Ionics* 2004, **172**, 591-595.
130. K. Maeda, *Phys. Chem. Chem. Phys.* , 2013, **15**, 10537-10548.
131. M. Yashima, Y. Lee and K. Domen, *Chem. Mater.* , 2007, **19**, 588-593.
132. G. Hitoki, T. Takata, J. N. Kondo, M. Hara, H. Kobayashi and K. Domen, *Chem. Commun.* , 2002, 1698-1699.
133. G. Hitoki, A. Ishikawa, T. Takata, J. N. Kondo, M. Hara and K. Domen, *Chem. Lett.* , 2002, **31**, 736-737.
134. T. Takata, G. Hitoki, J. N. Kondo, M. Hara, H. Kobayashi and K. Domen, *Res. Chem. Intermed.* , 2007, **33**, 13-25.
135. R. Nakamura, T. Tanaka and Y. Nakato, *J. Phys. Chem. B*, 2005, **109**, 8920-8927.
136. T. Hisatomi, M. Otani, K. Nakajima, K. Teramura, Y. Kako, D. Lu, T. Takata, J. N. Kondo and K. Domen, *Chem. Mater.* , 2010, **22**, 3854-3861.
137. L. Yuliati, J. Yang, X. Wang, K. Maeda, T. Takata, M. Antonietti and K. Domen, *J. Mater. Chem.* , 2010, **20**, 4295-4298.
138. Y. Fukasawa, K. Takanabe, A. Shimojima, M. Antonietti, K. Domen and T. Okubo, *Chem. Asian J.* , 2011, **6**, 103-109.
139. K. Nakajima, M. Hara, K. Domen and J. N. Kondo, *Chem. Lett.* , 2005, **34**, 394-395.
140. K. Kishida and T. Watanabe, *J. Solid State Chem.* , 2012, **191**, 15-18.
141. Z. Wang, J. Wang, J. Hou, K. Huang, S. Jiao and H. Zhu, *Mater. Res. Bull.* , 2012, **47**, 3605-3611.
142. K. Maeda, H. Terashima, K. Kase, M. Higashi, M. Tabata and K. Domen, *Bull. Chem. Soc. Jpn.* , 2008, **81**, 927-937.
143. K. Maeda, H. Terashima, K. Kase and K. Domen, *Appl. Catal., A*, 2009, **357**, 206-212.
144. I. Cimieri, H. Poelman, N. Avci, J. Geens, S. Lambert, B. Heinrichs and D. Poelman, *J. Sol-Gel Sci. Technol.* , 2012, **63**, 526-536.
145. K. Maeda, D. Lu and K. Domen, *Chem. Eur. J.*, 2013, **19**, 4986-4991.
146. H. Hagiwara, M. Nagatomo, C. Seto, S. Ida and T. Ishiahara, *Catalysts*, 2013, **3**, 614-624.
147. S. S. K. Ma, T. Hisatomi, K. Maeda, Y. Moriya and K. Domen, *J. Am. Chem. Soc.* , 2012, **134**, 19993-19996.
148. R. Abe, T. Takata, H. Sugihara and K. Domen, *Chem. Commun.* , 2005, 3829-3831.
149. M. Higashi, R. Abe, A. Ishikawa, T. Takata, B. Ohtani and K. Domen, *Chem. Lett.* , 2008, **37**, 138-139.
150. K. Maeda, M. Higashi, D. Lu, R. Abe and K. Domen, *J. Am. Chem. Soc.* , 2010, **132**, 5858-5868.
151. M. Tabata, K. Maeda, M. Higashi, D. Lu, T. Takata, R. Abe and K. Domen, *Langmuir*, 2010, **26**, 9161-9165.
152. K. Maeda, R. Abe and K. Domen, *J. Phys. Chem. C*, 2011, **115**, 3057-3064.
153. S. S. K. Ma, K. Maeda, T. Hisatomi, M. Tabata, A. Kudo and K. Domen, *Chem. Eur. J.*, 2013, **19**, 7480-7486.

154. M. Tsang, N. E. Pridmore, L. J. Gillie, Y. Chou, R. Brydson and R. E. Douthwaite, *Adv. Mater.* , 2012, **24**, 3406-3409.
155. Z. Wang, J. Hou, S. Jiao, K. Huang and H. Zhu, *J. Mater. Chem.* , 2012, **22**, 21972-21978.
156. Z. Wang, J. Hou, C. Yang, S. Jiao, K. Huang and H. Zhu, *Energy Environ. Sci.* , 2013, **6**, 2134-2144.
157. A. Ishikawa, T. Takata, J. N. Kondo, M. Hara and K. Domen, *J. Phys. Chem. B*, 2004, **108**, 11049-11053.
158. B. A. Pinaud, P. C. K. Vesborg and T. F. Jaramillo, *J. Phys. Chem. C*, 2012, **116**, 15918-15924.
159. M. Li, W. Luo, D. Cao, X. Zhao, Z. Li, T. Yu and Z. Zou, *Angew. Chem. Int. Ed.* , 2013, **52**, 11016-11020.
160. R. Abe, T. Takata, H. Sugihara and K. Domen, *Chem. Lett.* , 2005, **34**, 1162-1163.
161. R. Abe, M. Higashi and K. Domen, *J. Am. Chem. Soc.* , 2010, **132**, 11828-11829.
162. M. Higashi, K. Domen and R. Abe, *Energy Environ. Sci.* , 2011, **4**, 4138-4147.
163. E. S. Kim, N. Nishimura, G. Magesh, J. Y. Kim, J. Jang, H. Jun, J. Kubota, K. Domen and J. S. Lee, *J. Am. Chem. Soc.* , 2013, **135**, 5375-5383.
164. D. Yokoyama, H. Hashiguchi, K. Maeda, T. Minegishi, T. Takata, R. Abe, J. Kubota and K. Domen, *Thin Solid Films* 2011, **519**, 2087-2092.
165. C. M. Leroy, R. Sanjines, K. Sivula, M. Cornuz, N. Xanthopoulos, V. Laporte and M. Grätzel, *Energy Procedia*, 2012, **22**, 119-126.
166. H. X. Dang, N. T. Hahn, H. S. Park, A. J. Bard and C. B. Mullins, *J. Phys. Chem. C*, 2012, **116**, 19225-19232.
167. M. Higashi, K. Domen and R. Abe, *J. Am. Chem. Soc.* , 2012, **134**, 6968-6971.
168. M. Liao, J. Feng, W. Luo, Z. Wang, J. Zhang, Z. Li, T. Yu and Z. Zou, *Adv. Funct. Mater.* , 2012, **22**, 3066-3074.
169. Y. Cong, H. S. Park, H. X. Dang, F.-R. F. Fan, A. J. Bard and C. B. Mullins, *Chem. Mater.* , 2012, **24**, 579-586.
170. S. Banerjee, S. K. Mohapatra and M. Misra, *Chem. Commun.* , 2009, 7137-7139.
171. X. Feng, T. J. LaTempa, J. I. Basham, G. K. Mor, O. K. Varghese and C. A. Grimes, *Nano Lett.* , 2010, **10**, 948-952.
172. Y. Cong, H. S. Park, S. Wang, H. X. Dang, F.-R. F. Fan, C. B. Mullins and A. J. Bard, *J. Phys. Chem. C*, 2012, **116**, 14541-14550.
173. C. H. Wu, C. Hahn, S. B. Khan, A. M. Asiri, S. M. Bawaked and P. Yang, *Chem. Asian J.* , 2013, **8**, 2354-2357.
174. J. Hou, Z. Wang, C. Yang, H. Cheng, S. Jiao and H. Zhu, *Energy Environ. Sci.* , 2013, **6**, 3322-3330.
175. Y. Li, T. Takata, D. Cha, K. Takanabe, T. Minegishi, J. Kubota and K. Domen, *Adv. Mater.* , 2013, **25**, 125-131.
176. Y. Li, L. Zhang, A. Torres-Pardo, J. M. González-Calbet, Y. Ma, P. Oleynikov, O. Terasaki, S. Asahina, M. Shima, D. Cha, L. Zhao, K. Takanabe, J. Kubota and K. Domen, *Nat. Commun.*, 2013, **4**, 2566.
177. C. Zhen, L. Wang, G. Liu, G. Q. Lu and H. Cheng, *Chem. Commun.* , 2013, **49**, 3019-3021.
178. M. Liu, W. You, Z. Lei, T. Takata, K. Domen and C. Li, *Chin. J. Catal.* , 2006, **27**, 556-558.
179. M. Higashi, R. Abe, K. Teramura, T. Takata, B. Ohtani and K. Domen, *Chem. Phys. Lett.* , 2008, **452**, 120-123.

180. M. Higashi, R. Abe, T. Takata and K. Domen, *Chem. Mater.* , 2009, **21**, 1543-1549.
181. R. Sasaki, K. Maeda, Y. Kako and K. Domen, *Appl. Catal., B*, 2012, **128**, 72-76.
182. S. Ida, Y. Okamoto, M. Matsuka, H. Hagiwara and T. Ishihara, *J. Am. Chem. Soc.* , 2012, **134**, 15773-15782.
183. T. Matoba, K. Maeda and K. Domen, *Chem. Eur. J.*, 2011, **17**, 14731-14735.
184. K. Maeda and K. Domen, *Angew. Chem. Int. Ed.* , 2012, **51**, 9865-9869.
185. K. Ueda, H. Kato, M. Kobayashi, M. Hara and M. Kakihana, *J. Mater. Chem. A*, 2013, **1**, 3667-3674.
186. K. Maeda and K. Domen, *J. Phys. Chem. Lett.*, 2010, **1**, 2655-2661.
187. A. Murphy, P. Barnes, L. Randeniya, I. Plumb, I. Grey, M. Horne and J. Glasscock, *Int. J. Hydrogen Energy* 2006, **31**, 1999-2017.

Table 1. Ta_2O_5 photocatalysts for solar water splitting in the HPC system

Catalysts	Synthesis method	Cocatalyst (loading amount)	Light source	Reaction solution	Activity (μmol/h·g)		Ref.
					H_2	O_2	
Ta_2O_5 powder	Commercial	NiO_x (1 wt.%)	400 W Hg	Na_2CO_3	153	79	22
Ta_2O_5 powder	Commercial	NiO_x (1 wt.%)	400 W Hg	Pure water	190	99	22
Ta_2O_5 powder	Solvothermal	None	400 W Hg	2-Propanol	610	NA	23
Mesoporous Ta_2O_5	Ligand-assisted templating	NiO (4 wt.%)	450 W Hg	Pure water	1030	544	24
Mesoporous Ta_2O_5	Ligand-assisted templating and sol-gel	NiO (5 wt.%)	300 W Hg	Methanol	914.65	NA	25
Mesoporous Ta_2O_5	Ligand-assisted templating	NiO_x (3 wt.%)	450 W Hg	Pure water	11200[a]	5433 [a]	26
Ta_2O_5 powder	Commercial	NiO (1 wt.%)	300 W Hg	Methanol	588	NA	27
Ta_2O_5 powder	Commercial	NiO (1 wt.%)	300 W Hg	$AgNO_3$	NA	48	27
F doped Ta_2O_5 spheres	Co-precipitation and hydrothermal	None	NA	Methanol	52.4	NA	28
Fe doped Ta_2O_5	Sol-gel	Pt (1 wt.%)	350 W Xe	Methanol	700	NA	32
In_2O_3/Ta_2O_5	Sol-gel	Pt (1 wt.%)	300 W Xe	Methanol	3780	NA	33
CdS/Ta_2O_5	Evaporation-induced Self-assembly and ion-exchange	None	300 W Xe	Methyl blue	10814	NA	35
Ta_2O_5 nanotubes	Anodization	None	240 W Hg-Xe	Ethanol	4900 ± 320	NA	29
Ta_2O_5 hollow spheres	Layer-by-layer assembly	None	500 W Xe	Methanol	7100	NA	30
Ta_2O_5 hollow spheres	Templating	Ni/NiO	300 W Xe	Methanol	980	NA	31

a: activity of the 1st hour.

Table 2. Tantalate photocatalysts for solar water splitting in the HPC system

Catalysts	Synthesis method	Cocatalyst (loading amount)	Light source	Reaction solution	Activity (μmol/h·g)		Ref.
					H_2	O_2	
$KTaO_3$	Solid-state reaction	Ni (0.1 wt.%)	400 W Hg	Pure water	6	2	[37]
$Rb_4Ta_6O_{17}$	Solid-state reaction	Ni (0.1 wt.%)	400 W Hg	Pure water	92	46	[37]
$LiTaO_3$	Solid-state reaction	None	400 W Hg	Pure water	6	2	[38]
$NaTaO_3$	Solid-state reaction	None	400 W Hg	Pure water	4	1	[38]
$KTaO_3$	Solid-state reaction	None	400 W Hg	Pure water	29	13	[38]
$LiTaO_3$	Solid-state reaction	None	400 W Hg	Pure water	6.2	2.4	[40]
$LiTaO_3$	Solid-state reaction with 5% excess alkali	None	400 W Hg	Pure water	430	220	[40]
$LiTaO_3$	Solid-state reaction with 5% excess alkali	NiO (0.1 wt.%)	400 W Hg	Pure water	98	52	[40]
$NaTaO_3$	Solid-state reaction	None	400 W Hg	Pure water	11	4.4	[39, 40]
$NaTaO_3$	Solid-state reaction	NiO (0.05 wt.%)	400 W Hg	Pure water	480	240	[39, 40]
$NaTaO_3$	Solid-state reaction with 5% excess alkali	None	400 W Hg	Pure water	160	86	[39, 40]
$NaTaO_3$	Solid-state reaction with 5% excess alkali	NiO (0.05 wt.%)	400 W Hg	Pure water	2180	1100	[39, 40]
$KTaO_3$	Solid-state reaction	None	400 W Hg	Pure water	15	7	[40]
$KTaO_3$	Solid-state reaction	NiO (0.1 wt.%)	400 W Hg	Pure water	24	12	[40]
$KTaO_3$	Solid-state reaction with 10% excess alkali	None	400 W Hg	Pure water	29	13	[40]
$KTaO_3$	Solid-state reaction with 10% excess alkali	NiO (0.1 wt.%)	400 W Hg	Pure water	7.4	2.9	[40]
$NaTaO_3$	Hydrothermal	NiO (0.25 wt.%)	450 W Hg	Pure water	26666.7	13666.7	[42]

$NaTaO_3$	Hydrothermal	None	350 W Hg	Methanol	36750	NA	[43]
$NaTaO_3$	Microwave-assisted hydrothermal	NiO (0.4 wt.%)	450 W Hg	Pure water	~1100	~515	[44]
$Na_2Ta_4O_{11}$	Hydrothermal	None	400 W Hg	Pure water	6320[a]	NA	[45]
$Na_2Ta_4O_{11}$	Hydrothermal	None	400 W Hg	Methanol	37320[a]	NA	[45]
$NaTaO_3$	Hydrothermal	NiO (1.0 wt.%)	450 W Hg	Pure water	6666.7	3333.3	[46]
$Na_2Ta_2O_6$	Hydrothermal	NiO (0.2 wt.%)	450 W Hg	NaOH	782	390	[47]
$K_2Ta_2O_6$	Hydrothermal	NiO (0.2 wt.%)	450 W Hg	NaOH	874	452	[47]
$Na_2Ta_2O_6$	Hydrothermal	None	500 W Xe-Hg	Pure water	568	308	[48]
$KTaO_3$	Solid-state reaction	None	500 W Xe	KOH	2.0	NA	[49]
$KTaO_3$	Alkoxide method	None	500 W Xe	KOH	3.6	NA	[49]
$K_2Ta_2O_6$	Alkoxide method	None	500 W Xe	KOH	33.1	NA	[49]
$NaTaO_3$	Sol-gel	None	400 W Hg	Pure water	2050	1025	[50]
$NaTaO_3$	Sol-gel	None	400 W Hg	Pure water	2550	1300	[51]
$NaTaO_3$	Hydrothermal	None	400 W Hg	Pure water	700	350	[51]
$NaTaO_3$	Solid-state reaction	None	400 W Hg	Pure water	13.5	7	[51]
$K_3Ta_3Si_2O_{13}$	Solid-state reaction	NiO (1.3 wt.%)	400 W Hg	Pure water	368	188	[52]
$K_3Ta_3B_2O_{12}$	Solid-state reaction	None	450 W Hg	Pure water	4780	2420	[53]
$K_3Ta_3B_2O_{12}$	Aqueous solution-based process	NiO (0.2 wt.%)	450 W Hg	Pure water	784	384	[54]
$K_2PrTa_5O_{15}$	Solid-state reaction	NiO (0.5 wt.%)	400 W Hg	Pure water	517	23	[55]
$K_2SmTa_5O_{15}$	Solid-state reaction	NiO (0.5 wt.%)	400 W Hg	Pure water	623	272	[55]
$K_4Ce_2M_{10}O_{30}$	Solid-state reaction	NiOx (0.1 wt.%)	300 W Xe	Na_2SO_3	355	NA	[56]
$RbNdTa_2O_7$	Solid-state reaction	None	400 W Hg	Pure water	234.8	126.4	[57]
$RbNdTa_2O_7$	Solid-state reaction	Ni (0.5 wt%)	400 W Hg	Pure water	586.0	293.5	[58]
$NaNdTa_2O_7$	Solid-state reaction and ion exchange	Ni (0.5 wt%)	400 W Hg	Pure water	276.5	113.5	[60]

$HNdTa_2O_7$	Solid-state reaction and ion exchange	Ni (0.5 wt%)	400 W Hg	Pure water	26.5	11.5	[60]
$H_2SrTa_2O_7{\cdot}nH_2O$	Solid-state reaction and ion exchange	None	400 W Hg	Pure water	769	358	[61]
$K_2SrTa_2O_7{\cdot}nH_2O$	Solid state reaction	None	400 W Hg	Pure water	747	384	[61]
$H_2SrTa_2O_7{\cdot}nH_2O$	Solid-state reaction and ion exchange	None	400 W Hg	*n*-butylamine	2980	NA	[62]
$H_2La_{1/3}Ta_2O_7$	Solid-state reaction and ion exchange	NiO (2 wt.%)	400 W Hg	Pure water	1880	918	[63]
$NaCa_2O_3O_{10}$	Solid-state reaction and ion exchange	NiOx (0.5 wt.%)	400 W Hg	Pure water	1542	788.5	[64]
$LiCa_2O_3O_{10}$	Solid-state reaction and ion exchange	Ni (0.5 wt.%)	400 W Hg	Pure water	3540	1665	[65]
$Li_{0.23}Na_{0.77}Ca_2O_3O_{10}$	Solid-state reaction and ion exchange	Ni (0.5 wt.%)	400 W Hg	Pure water	3365	1550	[66]
$Li_7Ca_2O_3O_{10}$	Solid-state reaction and ion exchange	Ni (0.5 wt.%)	400 W Hg	Pure water	5840	2775	[67]
$K_{1.15}Ta_{0.92}Zr_{0.08}O_3$	Solid-state reaction	NiO (1.5 wt.%)	500 W Xe	Pure water	122.3	57.4	[68]
$KTa_{0.9}Hf_{0.1}O_{2.95}$	Solid-state reaction	NiO (1 wt.%)	500 W Xe	Pure water	98	40	[69]
$KTa_{0.92}Ti_{0.08}O_{2.96}$	Solid-state reaction	NiO (1 wt.%)	500 W Xe	Pure water	100	48	[69]
$NaTaO_3$: La	Solid-state reaction	NiO (0.05 wt.%)	400 W Hg	Pure water	5900	2900	[70]
$NaTaO_3$: La	Solid-state reaction	NiO (0.2 wt.%)	400 W Hg	Pure water	19800	9700	[72]
$NaTaO_3$: La	Sol-gel	None	400 W Hg	Methanol	2860	NA	[73]
$NaTaO_3$: La	Sol-gel	Ni (0.3 wt.%)	400 W Hg	Methanol	29200	NA	[74]
$NaTaO_3$: Ca (1 mol%)	Solid-state reaction	NiO (0.2 wt.%)	400 W Hg	Pure water	9860	5200	[76]
$NaTaO_3$: Sr (0.5 mol%)	Solid-state reaction	NiO (0.1 wt.%)	400 W Hg	Pure water	27200	13380	[76]
$NaTaO_3$: Ba (5 mol%)	Solid-state reaction	NiO (0.2 wt.%)	400 W Hg	Pure water	19560	9560	[76]
(Na, K)TaO_3: Zr (0.01	Molten-salt synthesis	None	350 W Hg	Pure water	46500	23100	[78]

mol%)							
(Na, K)TaO_3: Hf (0.02 mol%)	Molten-salt synthesis	None	350 W Hg	Pure water	49600	24900	[78]
Cynocobalamin/ $K_{0.95}Ta_{0.92}Ti_{0.08}O_3$	Solid-state reaction and impregnation method	None	500 W Xe	KOH	575.0	280.4	[79]
Rhodamine 6G/ $K_{0.95}Ta_{0.92}Ti_{0.08}O_3$	Solid-state reaction and evaporation	Pt	300 W Xe	KOH	833.5	295.0	[80]
$NaTa_{0.92}Cu_{0.08}O_3$	Solid-state reaction	NiO (0.3 wt.%)	300 W Xe	Methanol	10.4	NA	[81]
$NaTaO_3$: Ir Sr	Solid-state reaction	Pt (0.3 wt.%)	300 W Xe	Methanol	25	NA	[82]
$Na(Bi_{0.08}Ta_{0.92})O_3$	Hydrothermal	None	350 W Hg-Xe	Methanol	59.48	NA	[83]
$H_{1.9}K_{0.3}La_{0.5}Bi_{0.1}Ta_2O_7$	Polymerizable complex and proton exchange methods	None	300 W Hg	Pure water	2655	910	[84]
$NaTaO_3$: La	Solid-state reaction and photodeposition	Au (3 wt.%)	400 W Hg	Pure water	2820[b]	1220[b]	[87]
$NaTaO_3$: La	Solid-state reaction and impregnation	Au (3 wt.%)	400 W Hg	Pure water	7290[b]	3470[b]	[87]
$NaTaO_3$: La	Sol-gel	RuO2 (1.0 wt.%)	400 W Hg	Pure water	4108	1743	[88]
$NaTaO_3$	Solid-state reaction	$[Mo3S4]^{4+}$ (200 mol g^{-1})	450 W Hg	HCl	1700	850	[89]
$MgTa_2O_6$	Solid-state reaction	None	400 W Hg	Pure water	5	1	[38]
$BaTa_2O_6$	Solid-state reaction	None	400 W Hg	Pure water	33	15	[38]
$Sr_2Ta_2O_7$	Solid-state reaction	NiO (0.15 wt.%)	400 W Hg	Pure water	1000	480	[90, 91]
$Sr_2Ta_{1.5}Nb_{0.5}O_7$	Solid-state reaction	NiO (0.15 wt.%)	400 W Hg	Pure water	280	120	[91]
$SrTa_2O_6$	Solid-state reaction	NiO (0.1 wt.%)	400 W Hg	Pure water	960	490	[92]
$Sr_2Ta_2O_7$	Polymerizable complex	NiO (0.15 wt.%)	400 W Hg	Pure water	3517	1733	[93]
$Ba_5Ta_4O_{15}/Ba_{0.5}TaO_3$	Polymerizable complex	NiO (0.2 wt.%)	450 W Hg	Pure water	7110	3621	[94]
Mg-Ta mixed oxide	Ligand-assisted	NiO (0.1 wt.%)	450 W Hg	Pure water	333.3	166.7	[96, 97]

	templating and sol-gel						
$Sr_{0.5}TaO_3$	Direct dehydration	Ni (0.5 wt.%)	400 W Hg	Pure water	733	178	[98]
$Sr_{0.5}TaO_3$	Nanosheet processing	Ni (0.5 wt.%)	400 W Hg	Pure water	1400	489	[98]
$Sr_2Ta_2O_7$ nanosheets	Hydrothermal	NiO (0.15 wt.%)	350 W Hg	Pure water	5200	2560	[99]
$Ba_5Ta_4O_{15}/Ba_3Ta_5O_{15}$	Sol-gel citrate	Rh (0.025 wt.%)	350 W Hg	Methanol	1885	NA	[100]
$SrTa_2O_6$	Polymerizable complex	NiO (0.15 wt.%)	400 W Hg	Pure water	788[c]	404[c]	[101]
$Sr_4Ta_2O_9$	Polymerizable complex	NiO (0.15 wt.%)	400 W Hg	Pure water	64[c]	4[c]	[101]
$Sr_5Ta_4O_{15}$	Polymerizable complex	NiO (0.15 wt.%)	400 W Hg	Pure water	2388[c]	1444[c]	[101]
$SrBi_2Ta_2O_9$	Solid-state reaction	None	350 W Hg	Methanol	11300	NA	[102]
$H_{1.8}1Sr_{0.81}Bi_{0.19}Ta_2O_7$	Solid-state reaction and acid treatment	None	350 W Hg	Methanol	57670	NA	[103]
$H_{1.8}1Sr_{0.81}Bi_{0.19}Ta_2O_7$	Solid-state reaction and acid treatment	None	350 W Hg	Pure water	2460	1110	[103]
$Sr_2Ta_2O_{7-x}N_x$	Solid-state reaction	Pt (0.5 wt.%)	300 W Xe	Methanol	1940	NA	[104]
$Sr_2Ta_2O_{7-x}N_x$/graphene	Solid-state reaction and photoreduction	Pt (0.5 wt.%)	300 W Xe	Methanol	2930	NA	[103]
$Sr_2Ta_2O_{7-x}N_x$	Solid-state reaction	Co_x (1.0 wt.%)	300 W Xe	Methanol	NA	85.3	[105]
$Sr_5Ta_4O_{15-x}N_x$	Solid-state reaction	Pt (0.3 wt.%)	300 W Xe	Methanol	92.7	NA	[105]
$Ba_5Ta_4O_{15-x}N_x$	Solid-state reaction	Co_x (1.0 wt.%)	300 W Xe	$AgNO_3$	NA	132.7	[105]
$AgTaO_3$	Solid-state reaction	NiO (0.3 wt.%)	300 W Xe	Pure water	138.0	63.3	[106]
$Cd_2Ta_2O_7$	Sol-gel	NiO (0.2 wt.%)	300 W Hg	Pure water	576.7	287.7	[107]
$La_{1/3}TaO_3$	Solid-state reaction	Pt (0.5 wt.%)	400 W Hg	Methanol	122.14	NA	[108]
$InTaO_4$	Solid-state reaction	NiO_x (0.5 wt.%)	300 W Xe	Pure water	4.0	NA	[110-113]
$In_{0.8}Ni_{0.2}TaO_4$	Solid-state reaction	Pt (0.1 wt.%)	300 W Xe	Methanol	6.2	NA	[114, 115]
$In_{0.8}Ni_{0.2}TaO_4$	Solid-state reaction	Pt (0.1 wt.%)	300 W Xe	$AgNO_3$	NA	2.2	[114, 115]
$In_{0.90}Ni_{0.10}TaO_4$	Solid-state reaction	NiO (1.0 wt.%)	300 W Xe	Pure water	33.2	16.6	[116, 117]

$Sn_2Ta_2O_7$	Solid-state reaction	Pt	300 W Xe	Methanol	7.0	NA	[118]
$BiTa_{0.8}Nb_{0.2}O_4$	Solid-state reaction	Pt (0.1 wt.%)	400 W Hg	Pure water	41	NA	[121, 122]
Methylene blue-$BiTaO_4$	Solid-state reaction	Pt (0.3 wt.%)	500 W Hg-Xe	Isopropanol	4.1	NA	[123]

a: the unit of which is μl/g h; b: the unit of which is μmol/h; c: activity of the 1^{st} - 2^{nd} hour.

Table 3. Tantalum (oxy)nitride photocatalysts for solar water splitting in the HPC system

Catalysts	Synthesis method	Cocatalyst (loading amount)	Light source	Reaction solution	Activity (μmol/h·g)		Ref.
					H_2	O_2	
TaON	Nitridation	None	300 W Xe	$AgNO_3$	NA	1650[a]	132
TaON	Nitridation	Pt (3 wt.%)	300 W Xe	Methanol	11	NA	132
Ta_3N_5/La_2O_3	Nitridation	None	300 W Xe	$AgNO_3$	NA	2100[a]	133
Ta_3N_5	Nitridation	Pt (3 wt.%)	300 W Xe	Methanol	9	NA	133
Mesoporous Ta_3N_5	CVD and Nitridation	Pt (3 wt.%)	300 W Xe	Methanol	17	NA	136
Ta_3N_5	Templating and Nitridation	Pt (0.5 wt.%)	450 W Hg	Methanol	136	NA	137
Ta_3N_5	Templating and Nitridation	Pt (3 wt.%)	300 W Xe	Methanol	17.5	NA	138
Ta_3N_5	High pressure ammonothermal treatment	Pt (0.5 wt.%)	70 W Halide lamp	Methanol	72	NA	140
Ta_3N_5	Homogeneously chemical reduction	None	300 W Xe	$AgNO_3$	NA	2050	141
ZrO_2/Ta_3N_5	Solid solution reaction and nitridation	Ru (0.05 wt.%)	300 W Xe	Methanol	687.5	NA	142
$Zr_xTa_{1-x}O_{1+x}N_{1-x}$	Polymerizable complex method and nitridation	Ru (0.05 wt.%)	300 W Xe	Methanol	250	NA	143
ZrO_2/Ta_3N_5	Solid solution reaction and nitridation	Pt (0.5 wt.%)	300 W Xe	Methanol	445 ± 35	NA	144
ZrO_2/Ta_3N_5	Solid solution reaction and nitridation	RuO_x (3.0 wt.%)[b] Cr_2O_3 (2.5 wt.%)[b] IrO_2	450 W Hg	Pure water	15.0	6.7	145
Zn-TPP dimer/TaON	Nitridation	PtO_x (0.1 wt.%)	300 W Xe	Na_2S	956	1385	146
Na_2CO_3/ Ta_3N_5	Nitridation	CoO_x (2 wt.%)	300 W Xe	$AgNO_3$	NA	4550	147
Pt-TaON/Pt-WO_3	Nitridation	Pt (0.3 wt.%)-TaON/ Pt (0.5 wt.%)-WO_3	300 W Xe	NaI	60	30	148

Pt-TaON/Pt-WO_3	Nitridation	Pt (0.5 wt.%)-TaON/ Pt (0.5 wt.%)-WO_3	300 W Xe	NaI	5	2	[142]
Pt-ZrO_2-TaON/ Pt-WO_3	Nitridation	Pt (0.5 wt.%)-ZrO_2-TaON/ Pt (0.5 wt.%)-WO_3	300 W Xe	NaI	8.75	3.75	[142]
Pt-ZrO_2-TaON/ Pt-WO_3	Nitridation	Pt (0.5 wt.%)-ZrO_2-TaON/ Pt (0.5 wt.%)-WO_3	300 W Xe	NaI	100	50.7	[150]
Pt-ZrO_2-TaON/ Ir-TiO_2-Ta_3N_5	Nitridation	Pt (1 wt.%)-ZrO_2-TaON/ Ir (5 wt.%)-TiO_2®-WO_3	300 W Xe	NaI	20.0	8.5	[151]
Pt-TaON/ RuO_2-TaON	Nitridation	Pt(0.3 wt.%)-TaON/ RuO_2(0.3 wt.%)-TaON	300 W Xe	NaI	15	7	[149]
Pt-ZrO_2-TaON/ RuO_2-TaON	Nitridation	Pt (1 wt.%)-ZrO_2-TaON/ RuO_2 (0.5 wt.%)-TaON	300 W Xe	NaI	80	34	[152]
$SrTiO_3$:Rh/ Ir-CoO_x-Ta_3N_5	Nitridation	Ir(15 wt.%)-CoO_x(1 wt.%)-Ta_3N_5	300 W Xe	H_2SO_4	87.5	40	[153]
Macroporous TaON	Templating and Nitridation	None	300 W Xe	Methanol	212.5	NA	[154]
Macroporous Ta_3N_5	Templating and Nitridation	None	300 W Xe	Methanol	72.5	NA	[154]
Ta_3N_5 QDs/TaON	*In situ* chemical reduction	None	300 W Xe	$AgNO_3$	NA	1041	[155]
γ-TaON hollow urchin-like spheres	*In situ* self-assembly wet-chemical route	Ru (0.1 wt.%)	300 W Xe	Methanol	1272	NA	[156]
$SrTaO_2N$	Nitridation	Pt (3 wt.%)	300 W Xe	Methanol	100	NA	[129]
$LaTaON_2$	Nitridation	Pt (0.15 wt.%)/Ru (0.25 wt.%)	300 W Xe	Ethanol	126.7	NA	[178]

$CaTaO_2N$	Nitridation	Pt (0.3 wt.%)	300 W Xe	Methanol	83	NA	[181]
$Ca_2Ta_3O_{9.7}N_{0.2}$ nanosheet	Exfoliation	Rh (0.15 wt.%)	500 W Xe	Methanol	15610	NA	[182]
Pt-$BaTaO_2N$/Pt-WO_3	Nitridation	Pt (0.3 wt.%)-$BaTaO_2N$/Pt (0.5 wt.%)-WO_3	300 W Xe	NaI	35.0	16.7	[179, 180]
Pt-$BaZrO_3$-$BaTaO_2N$/ Pt-WO_3	Polymerizable complex method and nitridation	Pt (0.3 wt.%)-$BaZrO_3$-$BaTaO_2N$/Pt (0.5 wt.%)-WO_3	300 W Xe	NaI	36.7	20.0	[183]
$Na_{0.25}La_{0.75}TaO_{1.5}N_{1.5}$	Nitridation	Pt (0.3 wt.%)	300 W Xe	$AgNO_3$	NA	50	[185]
$Na_{0.25}La_{0.75}TaO_{1.5}N_{1.5}$	Nitridation	Pt (0.3 wt.%)	300 W Xe	Methanol	75	NA	[185]

a: activity of within the initial half hour; b; the content is metal-based.

Table 4. Tantalum (oxy)nitride photocatalysts for solar water splitting in the PEC system

Electrode[a]	Fabrication method	Reaction solution[b]	Light source	Photocurrent density (mA/cm^2)[c]	IPCE[d]	Ref.
Ta_3N_5/Ta	Oxidation and nitridation	KOH (pH 13.3)	1000 W Xe	0.5 at 1.5 V (RHE)	4.8%-540-1.57 V (RHE)	158
$Co(OH)_x$-Ta_3N_5/Ta	Oxidation and nitridation	NaOH (1 M)	NA	5.5 at 1.23 V (RHE)	50%-470-1.23 V (RHE)	159
IrO_2-TaON/FTO	Electrophoretic deposition	Na_2SO_4 (pH 6)	300 W Xe	3.8 at 0.6 V (Ag/AgCl)	76%-400-0.6 V (Ag/AgCl)	161
IrO_2-Ta_3N_5/FTO	Electrophoretic deposition	Na_2SO_4 (pH 6)	300 W Xe	3.8 at 0.6 V (Ag/AgCl)	31%-500-0.6 V (Ag/AgCl)	162
$CaFe_2O_4$-TaON/FTO	Electrophoretic deposition.	NaOH (pH 13.7)	300 W Xe	1.26 at 1.23 V (RHE)	30%-400-0.2 V(Ag/AgCl)	163
IrO_2-Ta_3N_5/Ta	Radio-frequency magnetron sputtering	Na_2SO_4 (pH 8.5)	300 W Xe	1.1 at 0.6 V (Ag/AgCl)	NA	164
TaO_xN_y/FTO	DC reactive sputtering	Na_2SO_4 (pH 7)	450 W Xe	0.029 at 1.23 V (RHE)	NA	165
Ta_3N_5/Ta	Reactive ballistic deposition	KOH (1 M)	Xe	2.4 at 0.6 V (Ag/AgCl)	2%-540-0.2 V(Ag/AgCl)	166
CoO_x-TaON/Ti	Electrophoretic deposition.	Na_3PO_4 (pH 8)	300 W Xe	3.4 at 1.2 V (RHE)	42%-400-1.2 V (RHE)	167
Co_3O_4-Ta_3N_5/FTO	Electrophoresis deposition	NaOH (pH 13.6)	500 W Xe	3.1 at 1.2 V (RHE)	24%-550-1.2 V (RHE)	168
$Ta_{0.6}Co_{0.4}N_x$	Drop casting and nitridation	Na_2SO_4 (pH 11)	150 W Xe	2.5 at 0.7 V (Ag/AgCl)	25%-450-0.6 V(Ag/AgCl)	169
TaON NTs/Ta[e]	Sonoelectrochemical anodization and nitridation	KOH (1 M)	300 W Xe	2.6 at 0.5 V (Ag/AgCl)	NA	170
Ta_3N_5 NTs/Ta[e]	Anodization and nitridation	KOH (1 M)	NA	NA	5.3%-450-0.5 V(Pt)	171
Co_3O_4-Ta_3N_5 NTs/Ta[e]	Anodization and nitridation	Na_2SO_4 (pH 11)	150 W Xe	1.3 at 0.7 V (Ag/AgCl)	9%-375-0.6 V(Ag/AgCl)	172

$Co(OH)_4$-Ta_3N_5 NRs/Ta[f]	Vapor-phase hydrothermal and nitridation	NaOH (pH 13.6)	NA	2.8 at 1.23 V (RHE)	37.8%-480-1.23 V (RHE)	177
Co_3O_4-$Co(OH)_2$-Ta_3N_5 NRs/Ta[f]	Vapor-phase hydrothermal and nitridation	Na_2SO_4 (pH 6.5)	150 W Xe	3.64 at 1.23 V (RHE)	39.5%-440-1.23 V (RHE)	174
IrO_2-Ta_3N_5 NWs/FTO[g]	Molten salt and nitridation	Na_2SO_4 (pH 6)	300 W Xe	0.6 at 1.5 V (RHE)	NA	173
IrO_2-Ta_3N_5 NRs/Ta[f]	Through-mask anodization	Na_2SO_4 (pH 13)	NA	3.8 at 1.23 V (RHE)	41.3%-440-1.23 V (RHE)	175
Co-Pi-Ba doped Ta_3N_5 NRs/Ta[f]	Through-mask anodization	K_2HPO_4 (pH 13)	NA	6.7 at 1.23 V (RHE)	55%-500-1.23 V (RHE)	176
IrO_2-TiO_2-$BaZrO_3$-$BaTaO_2N$/FTO	Electrophoretic deposition.	Na_2SO_4 (pH 5.9)	300 W Xe	0.03 at 1.2 V (RHE)	1.0%-500-1.2 V (RHE)	184

a: the content is in the form: cocatalysts-tantalum-based semiconductor/substrate; b: explanation between brackets is the pH or concentration of reaction solution; c: explanation between brackets represents the referring standard versus which the potential was measured; d: the content is in the form IPCE-wavelength-potential (referring standard); e: NTs refers to nanotubes; f: NRs refers to nanorods; g: NWs refers to nanowires.

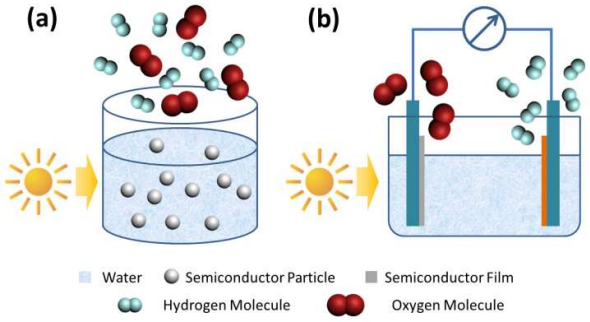

Scheme1. Schematic illustrations of two different semiconductor-based solar water splitting systems: (a) HPC system and (b) PEC system.

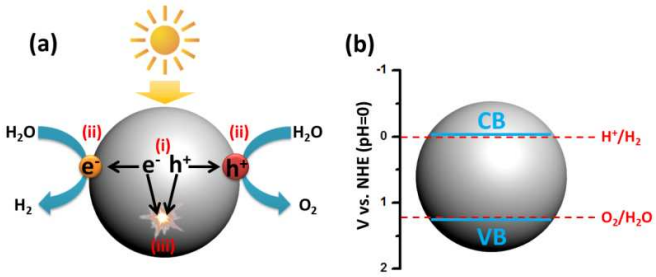

Scheme 2. (a) Schematic illustration of different processes during the solar water splitting, (i) (ii) (ii) in this scheme represent different processes during the solar water splitting: (i) generation of electron-hole pairs at irradiation of light, (ii) migration of charge carriers to the surface and HER/OER, (iii) recombination of unreacted electrons and holes; (b) schematic illustration of the band gap structure of semiconductors capable for overall solar water splitting.

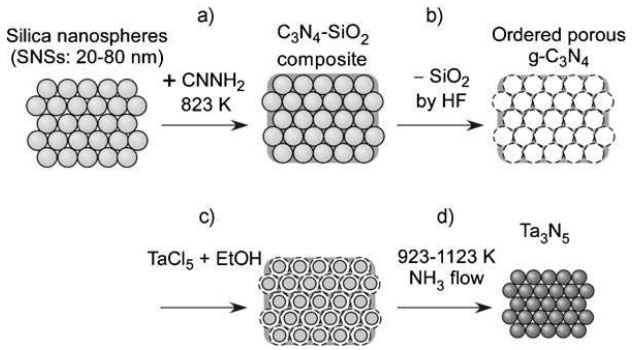

Scheme 3. Illustration of the synthesis of ordered porous graphic-C_3N_4 and regularly arranged Ta_3N_5 nanoparticles by using close-packed silica nanospheres as the primary template.[138]

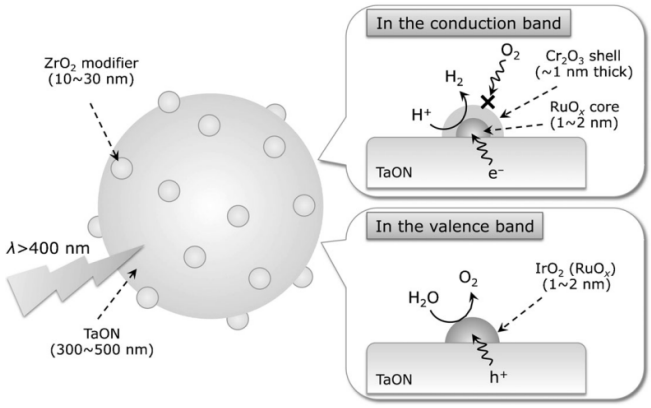

Scheme 4. Schematic illustration of the mechanism of overall water splitting on the $IrO_2/Cr_2O_3/RuO_x/ZrO_2/TaON$ photocatalyst.[145]

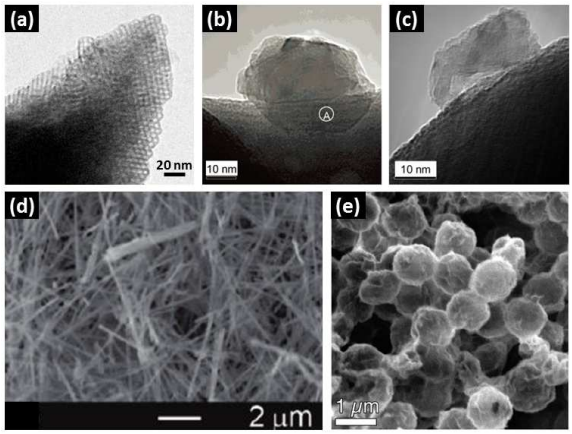

Fig. 1. (a) TEM image of crystallized mesoporous Ta_2O_5; TEM images showing the interface between NiO cocatalyst and Ta_2O_5 support in NiO/Ta_2O_5 photocatalyst obtained by (b) traditional thermal decomposition method and (c) cold plasma treatment; (d) SEM image of freestanding Ta_2O_5 nanotubes obtained by anodization; (e) TEM image of hollow Ta_2O_5 spheres synthesized using layer-by-layer method with PS spheres as the template.[26, 27, 29, 30]

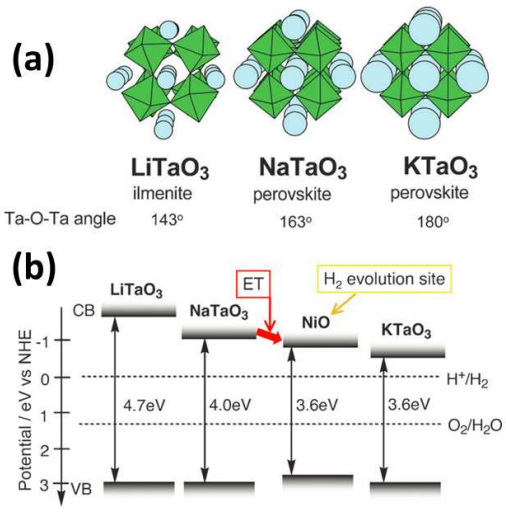

Fig. 2. (a) Crystal structures of alkali tantalates: $LiTaO_3$, $NaTaO_3$, $KTaO_3$; (b) band gap structures of alkali tantalates: $LiTaO_3$, $NaTaO_3$, $KTaO_3$ and NiO.[4, 40]

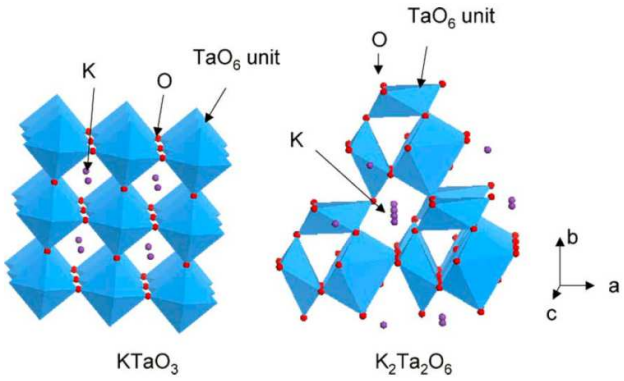

Fig. 3. Crystal structures of $KTaO_3$ and $K_2Ta_2O_6$.[49]

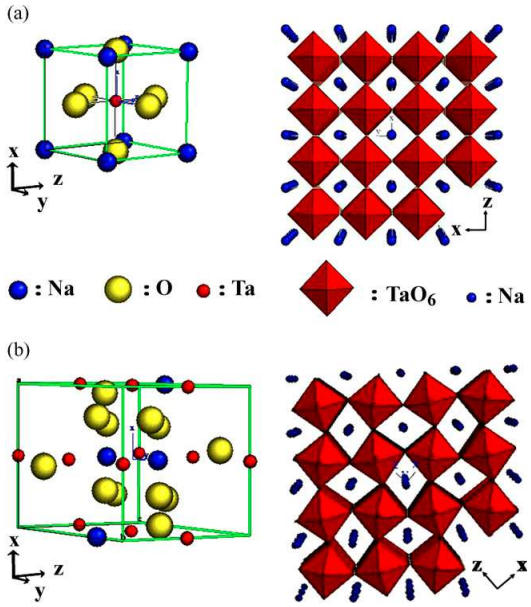

Fig. 4. The unit-cell and the refined crystalline structures of $NaTaO_3$ in the (a) monoclinic phase and (b) the orthorhombic phase.[50]

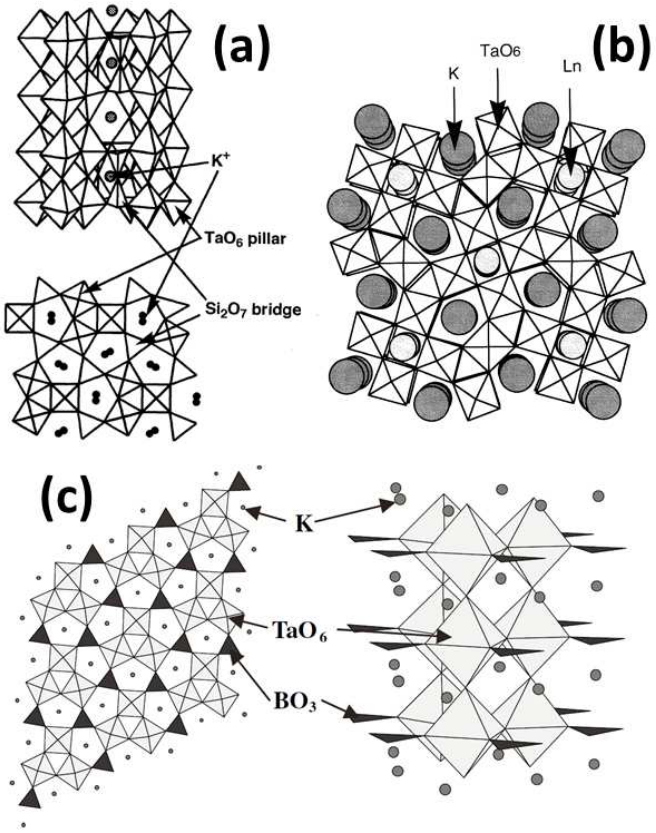

Fig. 5. Schematic illustrations of crystal structures of (a) $K_3Ta_3Si_2O_{13}$, (b) $K_2LnTa_5O_{15}$ and (c) $K_3Ta_3B_2O_{12}$.[52, 53, 55]

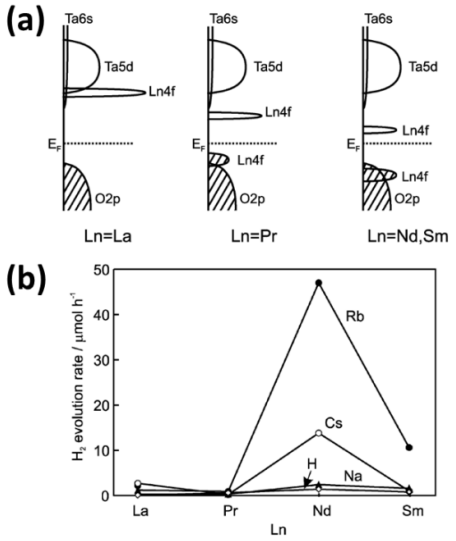

Fig. 6. (a) Schematic illustrations of band structures of $RbLnTa_2O_7$ (Ln = La, Pr, Nd and Sm) and (b) the rate of photocatalytic H_2 evolution from distilled water over $AA'Ta_2O_7$ (A = Cs, Rb, Na, and H; A' = La, Pr, Nd, and Sm).[60]

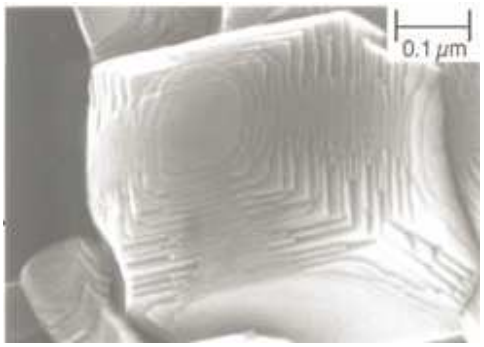

Fig. 7. SEM image of $NaTaO_3$: La (2%).[4]

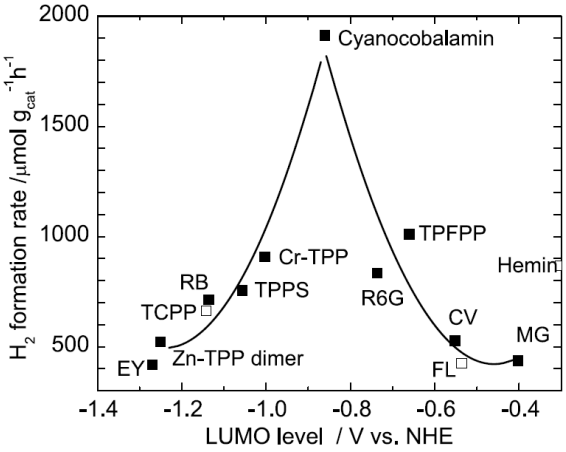

Fig. 8. Relationship between LUMO of dye and H_2 formation rate. EY: eosin Y; Zn-TPP dimer: pentamethylene bis[4-(10,15,20-triphenylporphin-5-yl)benzoate]dizinc(ll); TCPP: tetrakis(4-carboxyphenyl)porphine; RB: rose bengal; TPPS: tetraphenylporphine tetrasulfonic acid; Cr-TPP: Cr-tetraphenylporphyrin; R6G: rhodamine 6G; TPFPP: 5,10,15,20-tetrakis(pentafluorophenyl)-21H,23H-porphyrin; CV: crystal violet; FL: fluorescein; MG: malarchite green.[80]

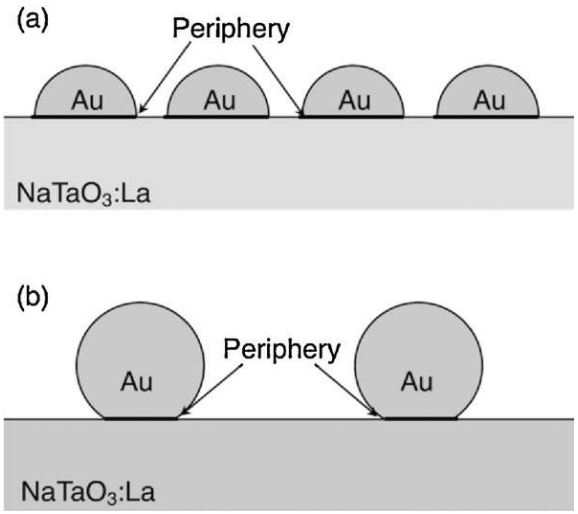

Fig. 9. Schematic views of (a) photodeposited and (b) impregnated Au on La-doped $NaTaO_3$.[87]

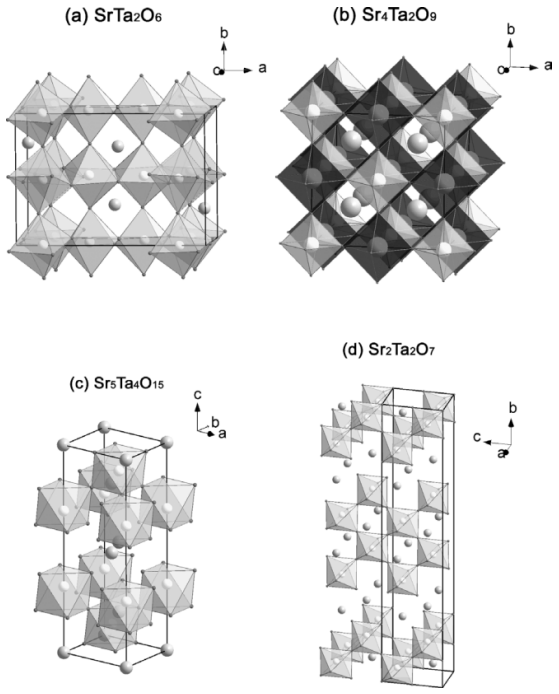

Fig. 10. Schematic illustrations of crystal structures of (a) $Sr_mTa_nO_{(m+\ 5n/2)}$: $SrTa_2O_6$, (b) $Sr_4Ta_2O_9$, (c) $Sr_5Ta_4O_{15}$ and (d) $Sr_2Ta_2O_7$.[101]

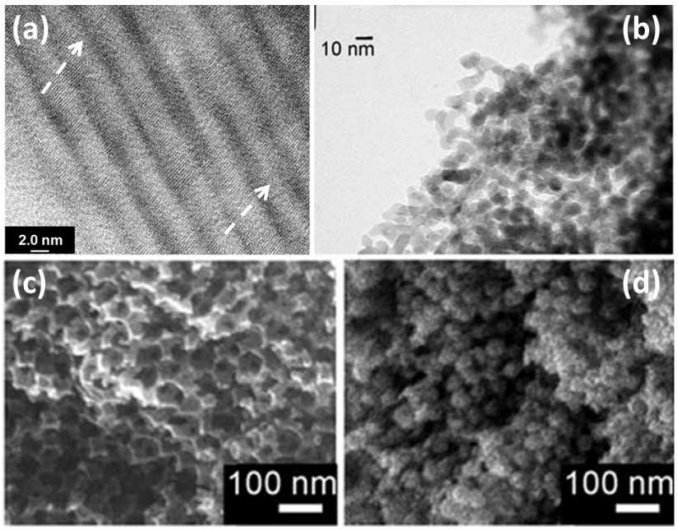

Fig. 11. (a) TEM image of ordered mesoporous Ta_3N_5; (b) TEM image of Ta_3N_5 particles obtained by using mesoporous C_3N_4 as the template; (c) SEM image of graphic-C_3N_4 obtained by using close-packed silica nanospheres as a primary template; (d) SEM image of Ta_3N_5 nanoparticles obtained by using graphic-C_3N_4 as the template.[136-138]

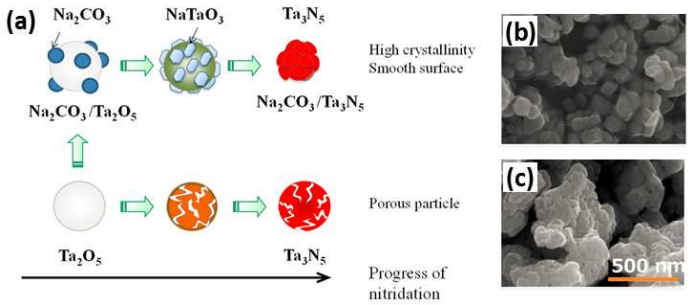

Fig. 12. (a) Scheme illustration of evolution of Na_2CO_3/Ta_3N_5 (top) and conventional Ta_3N_5 (bottom); (b) SEM images of Na_2CO_3/Ta_3N_5 and (c) conventional Ta_3N_5.[147]

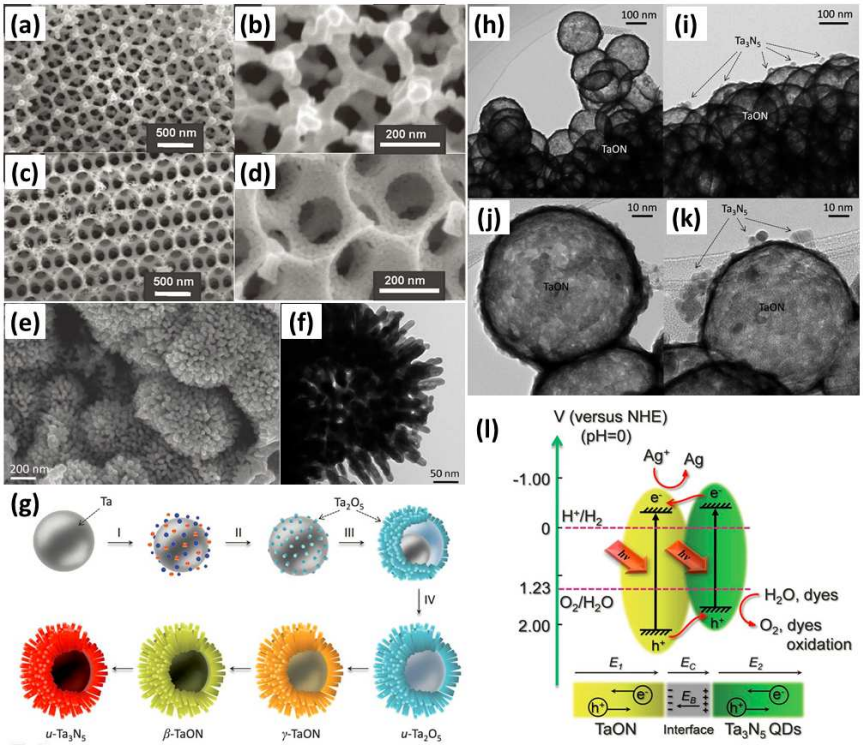

Fig. 13. (a, b) SEM images of macroporous TaON; (c, d) SEM images of macroporous Ta_3N_5; (e) SEM image of γ/β-TaON with urchin-like structure; (f) TEM image of γ-TaON with urchin-like structure; (g) schematic illustration of the formation process of hollow urchin-like u-Ta_2O_5 hierarchical nanostructures and with subsequent thermal nitridation successively forming γ-TaON, β-TaON and u-Ta_3N_5; TEM images of (h, j) TaON hollow spheres and (i, k) TaON hollow spheres coupled with Ta_3N_5 QDs; (l) schematic illustration of band gap energy diagram, electron-hole separation and transport of Ta_3N_5 QDs coupled TaON hollow spheres when irradiated with visible-light in both semiconductors.[154-156]

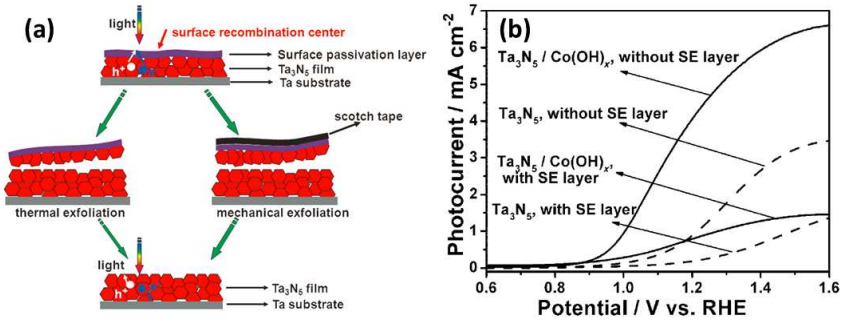

Fig. 14. (a) Mechanism of the photocurrent improvement after surface thermal and mechanical exfoliation; (b) I-V curves of Ta_3N_5/Ta photoanodes with and without $Co(OH)_x$ loading, before and after surface mechanical exfoliation (SE represent surface exfoliation).[159]

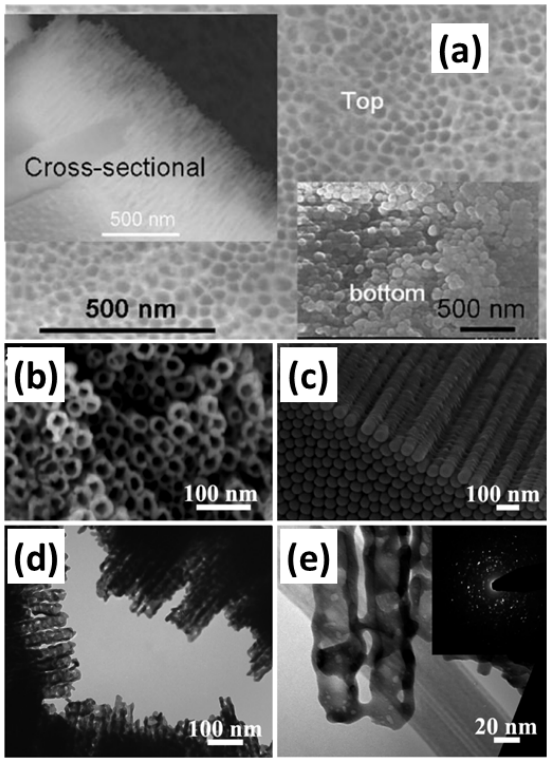

Fig. 15. (a) Top view SEM image of TaON nanotube arrays on a Ta foil with the inserts of cross-section view and bottom view SEM images; SEM images of Ta_3N_5 nanotube arrays viewed from (b) top and (c) bottom; TEM images Ta_3N_5 nanotube arrays with (d) low and (e) high magnification; and (insert of e) selected area electron diffraction pattern of Ta_3N_5.[170, 171]

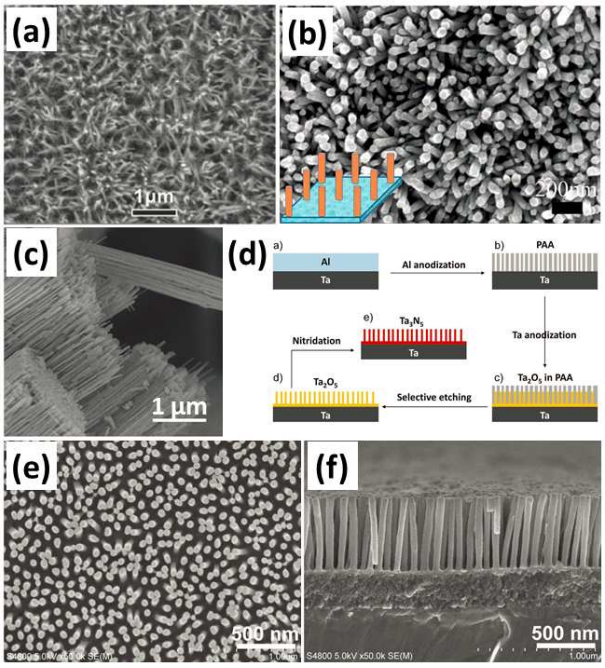

Fig. 16. (a, b and e) Top view SEM images of different Ta_3N_5nanorod arrays; (c) SEM image of Ta_3N_5 nanowire bundles; and (f) cross-section SEM image of Ta_3N_5nanorod arrays. (d) Schematic process for the fabrication of vertically aligned Ta_3N_5 nanorod arrays.[173, 175-177]

Table of content

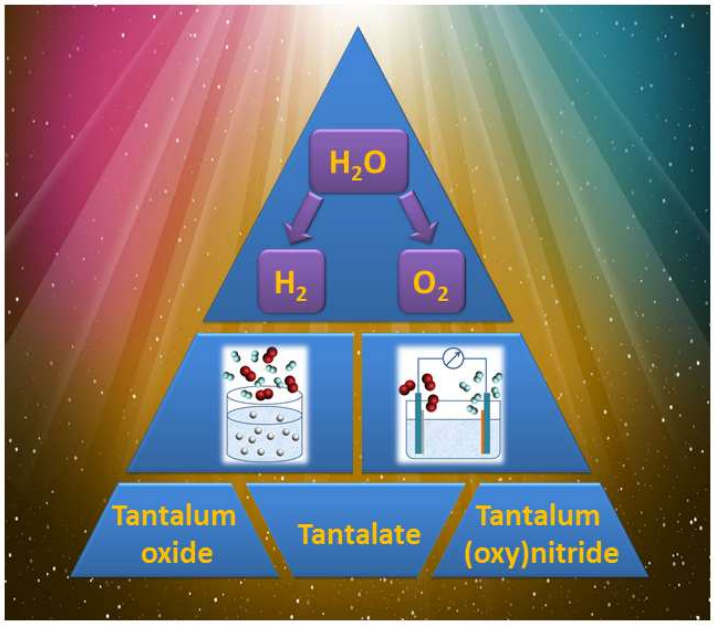

This review describes the current status of the design, synthesis, and applications of tantalum-based semiconductors, including tantalum oxides, tantalates and tantalum (oxy)nitrides, for photocatalytic and photoelectrochemical water splitting.

Peng Zhang received his bachelor degree in chemical engineering from Tianjin University in 2010. He is currently a PhD candidate in chemical engineering, supervised by Professor Jinlong Gong at Tianjin University. His research focuses on design of multifunctional materials for utilization of solar energy.

Jijie Zhang received his bachelor degree in molecular science and engineering from Tianjin University in 2012. Now he is a PhD candidate under the supervision of Professor Jinlong Gong at Tianjin University. His research focuses on solar energy conversion and utilization via heterogeneous photocatalysts.

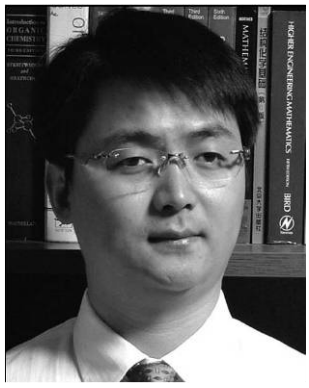

Jinlong Gong studied chemical engineering and received his B.S. and M.S. degrees from Tianjin University and his Ph.D. degree from the University of Texas at Austin under the guidance of C. B. Mullins. After a stint with Professor George M. Whitesides as a postdoctoral research fellow at Harvard University, he joined the faculty of Tianjin University, where he currently holds a Pei Yang Professorship in chemical engineering. He was a visiting scientist at the Pacific Northwest National Laboratory in 2007. He has served on the editorial boards for several journals including *Chemical Society Reviews* and *Chemical Science*. He is an elected Fellow of the Royal Society of Chemistry (FRSC). His research interests in surface science and catalysis include catalytic conversions of green energy, novel utilizations of carbon dioxide, and synthesis and applications of nanostructured materials.